

Gradient-consistent enrichment of finite element spaces for the DNS of fluid-particle interaction

Susanne Höllbacher^{a,b,*}, Gabriel Wittum^{a,b}

^a*King Abdullah University of Science and Technology (KAUST), Extreme Computing Research Center (ECRC), Computer, Electrical and Mathematical Sciences and Engineering (CEMSE), Thuwal, 23955-6900, Kingdom of Saudi Arabia*

^b*Goethe-Center for Scientific Computing (G-CSC), Johann Wolfgang Goethe University, Kettenhofweg 39, 60423 Frankfurt, Germany*

Abstract

We present gradient-consistent enriched finite element spaces for the simulation of free particles in a fluid. This involves forces being exchanged between the particles and the fluid at the interface. In an earlier work [23] we derived a monolithic scheme which includes the interaction forces into the Navier-Stokes equations by means of a fictitious domain like strategy. Due to an inexact approximation of the interface oscillations of the pressure along the interface were observed. In multiphase flows oscillations and spurious velocities are a common issue. The surface force term yields a jump in the pressure and therefore the oscillations are usually resolved by extending the spaces on cut elements in order to resolve the discontinuity. For the construction of the enriched spaces proposed in this paper we exploit the Petrov-Galerkin formulation of the vertex-centered finite volume method (PG-FVM), as already investigated in [23]. From the perspective of the finite volume scheme we argue that wrong discrete normal directions at the interface are the origin of the oscillations. The new perspective of normal vectors suggests to look at *gradients* rather than *values* of the enriching shape functions. The crucial parameter of the enrichment functions therefore is the gradient of the shape functions and especially the one of the *test* space. The distinguishing feature of our construction therefore is an enrichment that is based on the choice of shape functions with consistent gradients. These derivations finally yield a fitted scheme for the immersed interface. We further propose a strategy ensuring a well-conditioned system independent of the location of the interface. The enriched spaces can be used within any existing finite element discretisation for the Navier-Stokes equation. Our numerical tests were conducted using the PG-FVM. We demonstrate that the enriched spaces are able to eliminate the oscillations.

Keywords: immersed boundary method, monolithic scheme, enriched finite elements, Petrov-Galerkin finite volumes, spurious pressure

*Corresponding author

Email address: susanne.hoellbacher@gcsc.uni-frankfurt.de (Susanne Höllbacher)

1. Introduction

Particulate flows are one of many applications in engineering and biology involving immersed interfaces moving in time within the *fluid region*. Examples range from electrostatics and diffusion problems to elasticity and fluid dynamics. In the case of a moving interface it can be reasonable to avoid expensive re-meshing and it has become a popular strategy to allow the interface to cut the elements of the mesh. These so called immersed boundary methods (IBM) are a good alternative to ease the representation of the geometry. Since an IBM does not require the interface to align the underlying grid, the main challenge is to capture the phenomena on the free boundary by suitable adaptations of the discrete scheme.

The original IBM was formulated by Peskin [34]. New *Lagrangian points* (LP) are defined along the interface. Since the singular forces arising at the interface can be understood as delta functions, Peskin introduces suitable *discrete* delta functions (DDF) for the Lagrangian points which spread the forces into the surrounding domain. The discontinuity will be smoothed out and therefore one drawback is a *low* accuracy. In [40] and [41] a generalized IBM with higher order approximation is developed.

The discrete delta function acts as a link between the moving interface and fixed Eulerian grid. Since it employs explicit expressions for the body force, it is categorized into the class of *direct forcing* schemes. A good overview is given in [29]. In the context of finite difference methods the *ghost fluid method*, introduced for compressible flow by Fedkiw et al. [11], is a popular direct forcing approach to include the moving interface into the Euler frame of reference. Further examples for direct forcing for finite volume schemes are those of Uhlmann [43] and Breugem [6] who developed a direct forcing strategy for particulate flows.

In this paper, we will focus on the class of immersed boundary methods which introduce the boundary condition in a weak sense (*weak forcing*). Within the finite element framework the *extended finite element method* (XFEM) is the most prominent example. Moës et al. [30] first introduced the XFEM method to model the discontinuities without adapting the grid to the interface. Instead, the finite element spaces are enriched by additional shape functions. In [35] and [17] XFEM is applied to flow problems in order to model the discontinuity of the pressure. In the recent work of Kirchhart et al. [25] theoretical analysis of the XFEM is applied to the interface Stokes problem.

Another extended finite element technique is the CutFEM method by Hansbo and Hansbo [19]. Based on Nitsche's method, cf. [32], enrichment functions are utilised to impose the interface conditions weakly and penalty terms are introduced to stabilize the system. CutFEM was first derived for the elliptic interface problem by Hansbo and Hansbo [19], later Becker et al. [4] and Hansbo et al. [21] developed the method for a Stokes interface problem and in [20], [7] the weak coupling approach was applied to fluid-structure interaction. In [7] the problem of pressure oscillation at the interface is treated by introducing penalty terms.

Within the context of finite volume methods (FVM) we already referred to the direct forcing method of Uhlmann [43] for particulate flows. We want to mention the class of so called *cut cell* methods and especially the one for elliptic problems by Oevermann et al. [33] since he combines the finite volume scheme with finite element techniques which is comparable to our approach. The local finite element spaces are utilised for interpolation on the cut cells.

The immersed boundary method derived in this work introduces gradient-consistent enriched finite element spaces in order to capture the boundary conditions at the interface. It can therefore be categorised as an extended method sharing many similarities with the spaces applied by CutFEM. A distinguishing feature of our proceeding however is the construction of a suitable enrichment of the trial and test spaces by exploiting the Petrov-Galerkin formulation of the vertex-centered finite volume method. For the formulation of a vertex-centered FVM (also known as *finite volume-element method or box method* [3]) usually a second, dual mesh is introduced. Using first-order conforming trial functions on the primal mesh (given triangulation) and piecewise constant test functions on the corresponding dual mesh the FVM can be formulated in variational form (Petrov-Galerkin method). Therefore we will further refer to it as a *Petrov-Galerkin* finite volume method (PG-FVM).

In view of the application to particulate flows and more generally multiphase flows,

we emphasize the main difference of our enrichment strategy via the PG-FVM to other approaches: For multiphase flows a good resolution of the interface is necessary to avoid spurious oscillations of velocity and pressure. These are caused by bad approximations of the interface forces. Since the surface forces lead to a jump in the pressure value, in common XFEM strategies for two phase flows the enrichment aims at capturing the discontinuity of the pressure, see e.g. [36], [16], [21], [2], [10]. From the perspective of the PG-FVM (inheriting normal fluxes in the discrete formulation) the bad approximation of interface forces can be traced back to the error in the discrete normal directions. As a consequence, our enrichment aims at capturing the normal directions and with it the gradients of the *test* space appropriately. A detailed explanation for the relation between normal directions and test space gradients will be given in Section 3. The request for consistent gradients finally yields enrichments functions, which possess the Kronecker-delta property with respect to the interface. Moreover, we constrain our spaces to form a partition of unity (PU). As a result, the gradient-consistent spaces are constructed via a combination of a *projection* (Kronecker-delta property) and *reduction* (PU property) rather than *extension* and *restriction* as done in [16] or [21]. The proposed enrichment of the spaces can be similarly applied to both, a Galerkin FEM or a PG-FVM for the Navier-Stokes equations. We emphasize that another common FV discretisation, the so-called *cell-centered* FVM, follows another approach. The technique which will be derived in this paper refers to the vertex-centered scheme.

We finally propose a strategy to avoid ill-conditioning on cut elements. Common extended finite element approaches need to handle this issue for "small" cut elements for which the volume on one of the parts of the cut element gets very small. In [21] stabilization terms for the velocity and the pressure guarantee a well conditioned system matrix.

Similar stabilisation terms are applied in [25]. Ill-conditioning is similarly an issue for the proposed spaces. In contrast to small support on cut elements only cut elements impairing the shape-regularity of the mesh are critical. Instead of adding stabilization terms we slightly adjust the linear system by means of geometrical reasoning preserving the optimal order of convergence. Moreover, the choice of spaces maintains symmetry. Consequently, stability results can be derived easily without the necessity to introduce additional penalisation or stabilisation terms.

The oscillations observed in our unfitted scheme in [23] could be eliminated due to the suitable enrichment of the spaces. Our method does not comprise numerical fluxes as artifact.

The paper is organized as follows: In Section 2 we introduce the model problem
95 and the discrete operators for both, a general Galerkin FEM and the Petrov-Galerkin
FVM. Section 3 explains from the perspective of gradients why an unfitted method
produces oscillations. This serves as motivation for the construction of the gradient-
consistent spaces in Section 4. Herein, the proposed enrichment will be combined with
the rotational spaces introduced in [23] for its application to particulate flows. Section
100 5 summarizes some important properties of the enriched spaces. In Section 6 theoretical
results regarding conditioning and stability will be derived. Finally, we present numerical
results in Section 7 which demonstrate the elimination of the oscillations as well as the
optimal order of convergence.

2. Mathematical Formulation

105 2.1. Governing equations

Let $\Omega \subset \mathbb{R}^d$, with $d = 2, 3$, be a polyhedral domain. For simplification of the notation
we will take only one particle $P \subset \Omega$ into consideration and presume it to have a spherical
shape. All derivations can be applied to each further particle. The domain occupied by
the fluid will be denoted by $\Omega_f := \Omega \setminus P$, see Fig. 1. We assume an incompressible and
110 Newtonian fluid and therefore the equations that govern the flow are the Navier-Stokes
equations in Ω_f :

$$\rho_f \left(\frac{\partial}{\partial t} \mathbf{u} + \mathbf{u} \cdot \nabla \mathbf{u} \right) = \nabla \cdot \boldsymbol{\sigma} + \mathbf{g} \quad \text{in } \Omega_f, \quad (1)$$

$$\nabla \cdot \mathbf{u} = 0 \quad \text{in } \Omega_f, \quad (2)$$

$$\mathbf{u} = \mathbf{U} + \boldsymbol{\omega} \times \mathbf{r}(\vec{x}) \quad \text{on } \partial P, \quad (3)$$

$$\mathbf{u} = \mathbf{u}_D \quad \text{on } \partial \Omega, \quad (4)$$

with stress tensor $\boldsymbol{\sigma} := -p \mathbf{I} + \mu_f (\nabla \mathbf{u} + \nabla \mathbf{u}^T)$, viscosity μ_f and density ρ_f of the fluid and
given Dirichlet values \mathbf{u}_D . We will presume constant fluid density. As already anticipated
by the notation the volume force \mathbf{g} will only be exerted by gravitation in all considered
115 problems.

The particles arise as a boundary condition (3) in the equations of the fluid. Since
their motion is assumed to be rigid, their velocity is composed accordingly by a translational
component $\mathbf{U} \in \mathbb{R}^d$ and angular component $\boldsymbol{\omega} \in \mathbb{R}^d$. The motion can be described
by the Newton-Euler equations and therefore \mathbf{U} and $\boldsymbol{\omega}$ obey the relation

$$M_P \frac{d}{dt} \mathbf{U} = \mathbf{F}_H + M_P \mathbf{g}, \quad I_P \frac{d}{dt} \boldsymbol{\omega} = \mathbf{T}_H, \quad (5)$$

with \mathbf{F}_H and \mathbf{T}_H being the hydrodynamic force and torque

$$\mathbf{F}_H = \int_{\partial P} \boldsymbol{\sigma}(\vec{x}) \mathbf{n} \, ds, \quad \mathbf{T}_H = \int_{\partial P} \mathbf{r}(\vec{x}) \times \boldsymbol{\sigma}(\vec{x}) \mathbf{n} \, ds, \quad (6)$$

acting on the center of mass of the particle.

Remark 1 (Full stress tensor). We emphasize that the viscous terms in (5) and (6)
depend on the complete stresses. As a consequence, the viscous dissipation in (1) for
the fluid in the proximity of a particle equally needs to be modeled by the complete stress
tensor rather than by the more common term $\nabla \mathbf{u}$, see also [14].
120

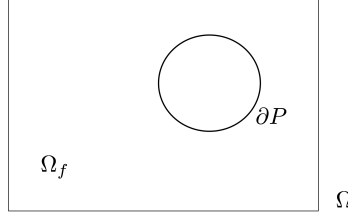


Figure 1: Computational domain for the particulate flow problem comprising one embedded particle P .

2.2. Discrete equations for the fluid: Weak formulation using linear finite element spaces

The weak formulation of (1) - (2) without particles and a suitable choice of discrete spaces for velocity and pressure yields a finite element method for the Navier-Stokes equations. We define

$$\mathcal{V}_{h,D}^k := \{v \in \mathcal{P}^k(\mathcal{T}_h) : v|_{\partial\Omega} = u_D\}, \quad \mathcal{Q}_h^l := \{p \in \mathcal{P}^l(\mathcal{T}_h) : \int_{\Omega_f} p \, d\mathbf{x} = 0\},$$

and $\mathbf{V}_{h,D}^k := [\mathcal{V}_{h,D}^k]^d$ with $\mathcal{P}^k(\mathcal{T}_h)$, $\mathcal{P}^l(\mathcal{T}_h)$, $k, l \in \mathbb{N}$ being the common spaces of piecewise polynomial functions w.r.t. a given simplicial decomposition \mathcal{T}_h of Ω . Since our approach is based on the association of the Galerkin FEM with the corresponding PG-FVM we will concentrate on FE schemes with piecewise linear spaces for the velocity and piecewise constant spaces for the pressure.

Finite element scheme: The weak form of (1) - (2) reads: Find $(\mathbf{u}, p) \in (\mathbf{V}_{h,D}^1, \mathcal{Q}_h^0)$ s.t.

$$a_{\text{FE}}(\mathbf{u}, \mathbf{v}) + b_{\text{FE}}(\mathbf{v}, p) = (\mathbf{g}, \mathbf{v}) \quad \forall \mathbf{v} \in \mathbf{V}_{h,0}^1, \quad (7)$$

$$b_{\text{FE}}(\mathbf{u}, q) + s_{\text{FE}}(q, q) = 0 \quad \forall q \in \mathcal{Q}_h^0. \quad (8)$$

with bilinear forms

$$a_{\text{FE}}(\mathbf{u}, \mathbf{v}) := \rho \int_{\Omega} \frac{d}{dt} \mathbf{u} \cdot \mathbf{v} \, d\mathbf{x} + \int_{\Omega} 2\mu \mathbf{D}[\mathbf{u}] : \mathbf{D}[\mathbf{v}] \, d\mathbf{x}, \quad (9)$$

$$b_{\text{FE}}(\mathbf{v}, p) := - \int_{\Omega} p \nabla \cdot \mathbf{v} \, d\mathbf{x}, \quad (10)$$

the L^2 -inner product

$$(\mathbf{g}, \mathbf{v}) := \int_{\Omega} \mathbf{g} \cdot \mathbf{v} \, d\mathbf{x}$$

and the rate-of-strain tensor $\mathbf{D}[\mathbf{u}] := 0.5(\nabla \mathbf{u} + \nabla \mathbf{u}^T)$. Due to Remark 1 the weak formulation involves $\mathbf{D}[\mathbf{u}] : \mathbf{D}[\mathbf{v}]$ instead of the more usual term $\nabla \mathbf{u} : \nabla \mathbf{v}$.

A suitable stabilisation $s_{\text{FE}}(\cdot, \cdot)$ might be necessary. As this will not be part of this paper we shall not comment on the specific definition of this term.

Finite volume scheme: Choosing different trial and test spaces yields so-called *Petrov-Galerkin* schemes. The choice of piecewise constant test functions introduces additional boundary integrals in the weak formulation (as in the context of DG schemes) and leads to the following finite volume scheme: Find $(\mathbf{u}, p) \in (\mathbf{V}_{h,D}^1, \mathcal{Q}_h^1)$ s.t.

$$a_{\text{FV}}(\mathbf{u}, \mathbf{v}) + b_{\text{FV}}(\mathbf{v}, p) = (\mathbf{g}, \mathbf{v}) \quad \forall \mathbf{v} \in \bar{\mathbf{V}}_{h,D}, \quad (11)$$

$$b_{\text{FV}}(\mathbf{u}, q) + s_{\text{FV}}(q, q) = 0 \quad \forall q \in \bar{\mathcal{Q}}_h, \quad (12)$$

¹²⁵ with bilinear forms

$$a_{\text{FV}}(\mathbf{u}, \mathbf{v}) := \sum_i \left(\rho \int_{B_i} \frac{d}{dt} \mathbf{u} \cdot \mathbf{v} \, d\mathbf{x} - \int_{\partial B_i} \mu(\nabla \mathbf{u} + \nabla \mathbf{u}^T) \mathbf{n} \cdot \mathbf{v} \, ds \right), \quad (13)$$

$$b_{\text{FV}}(\mathbf{v}, p) := \sum_i \int_{\partial B_i} p \mathbf{n} \cdot \mathbf{v} \, ds, \quad (14)$$

and the function space of piecewise constants on each $B_i \in \mathcal{B}_h$ defined as

$$\bar{\mathcal{V}}_{h,D} := \{v \in \mathcal{P}^0(\mathcal{B}_h) : v|_{\partial\Omega} = u_D\}, \quad \bar{\mathcal{Q}}_h := \{p \in \mathcal{P}^0(\mathcal{B}_h) : \int_{\Omega_f} p \, d\mathbf{x} = 0\} \quad (15)$$

¹³⁰ and $\bar{\mathbf{V}}_{h,D} := [\bar{\mathcal{V}}_{h,D}]^d$. We emphasize that the set of so-called *control volumes* $\mathcal{B}_h := \{B_i\}_i$ is assumed to form a partition of the domain Ω , but not necessarily is a simplicial decomposition or even identical with \mathcal{T}_h . An exact definition for the PG-FVM applied in this paper will be given in the following. We again do not comment on the specific definition of the term $s_{\text{FV}}(\cdot, \cdot)$.

We finally introduce the following notations for the stresses within the Galerkin and Petrov-Galerkin formulation. With

$$c_{\text{FE}}^{\text{cpl}}(\mathbf{u}, \mathbf{v}) := \int_{\Omega} 2\mu \mathbf{D}[\mathbf{u}] : \mathbf{D}[\mathbf{v}] \, d\mathbf{x}$$

and

$$c_{\text{FV}}^{\text{cpl}}(\mathbf{u}, \mathbf{v}) := - \sum_i \int_{\partial B_i} \mu(\nabla \mathbf{u} + \nabla \mathbf{u}^T) \mathbf{n} \cdot \mathbf{v} \, ds$$

we define $c_{\text{FE/FV}}(\mathbf{u}, p; \mathbf{v}) := c_{\text{FE/FV}}^{\text{cpl}}(\mathbf{u}, \mathbf{v}) + b_{\text{FE/FV}}(\mathbf{v}, p)$. The notation '*cpl*' shall emphasize that the according terms are responsible for the coupling between the degrees of freedom of the fluid and the particle, as described in [23] in more detail.

For all numerical tests in Section 7 we applied the vertex-centered PG-FVM using so-called *barycentric* control volumes B_i . Each B_i is constructed around the vertex $\vec{x}_i \in \mathcal{T}_h$ by connecting the barycenters of all neighbouring edges, faces and volumes to a convex hull enclosing \vec{x}_i (see Fig. 2). The *characteristic* functions $\chi_i(\vec{x})|_{B_i} \equiv 1$, $\chi_i(\vec{x}) \equiv 0$ else, for all $B_i \in \mathcal{B}_h$ form a basis of the test space $\bar{\mathcal{V}}_{h,1}$ and by construction we can define a bijective mapping $\Pi : \mathcal{V}_{h,1}^1 \rightarrow \bar{\mathcal{V}}_{h,1}$, $\Pi(\varphi_i) := \chi_i$ between the basis of the Galerkin and Petrov-Galerkin test spaces. For this special choice of control volumes the resulting Petrov-Galerkin scheme is known to satisfy

$$\int_{\partial B_i} \nabla u \cdot \mathbf{n} \, ds = - \int_{\Omega} \nabla u \cdot \nabla \varphi_i \, d\mathbf{x}, \quad (16)$$

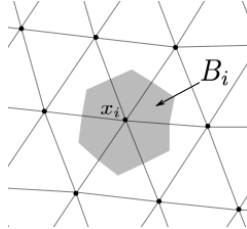


Figure 2: Vertex-centered PG-FVM (*box method* [3]) with *barycentric* control volume B_i associated to the vertex \vec{x}_i .

for $u, \varphi_i \in \mathcal{P}^1(\mathcal{T}_h)$ and normalized test function $\varphi_i(\vec{x}_i) = 1$. Therefore, it reproduces the stiffness matrix for the Laplace (assuming piecewise constant coefficients on each triangle) provided that linear finite elements are used. The equality (16) was first proven by Bank and Rose [3] for the two-dimensional case and later also for arbitrary dimension by Chen [8], Xu and Zou [50] and Hackbusch [18].

Identifying finite element and finite volume schemes: The identification (16) between the Galerkin FEM and the PG-FVM was already used for the formulation of the FEM for particulate flows in [23]. By means of (16) the following identity between the stress terms was derived therein:

$$c_{\text{FE}}(\mathbf{u}, \Pi(p); \mathbf{v}) = c_{\text{FV}}(\mathbf{u}, p; \Pi(\mathbf{v})) + R(h), \quad (17)$$

on the according spaces. $R(h) = 0$ directly follows from (16) in the case of a simplicial mesh and an elementwise constant pressure. In [52] the estimate $c_{\text{FE}}^{\text{cpl}}(\mathbf{u}, \mathbf{v}) = c_{\text{FV}}^{\text{cpl}}(\mathbf{u}, \mathbf{v}) + R(h)$ for the coupling terms, with $R(h) = O(h^2)$, was derived for triangular and rectangular meshes. The only requirement is a piecewise constant approximation of the viscosity w.r.t. the mesh \mathcal{T}_h .

In Section 3 we will explain the origin of the oscillations of the pressure in order to derive appropriate new function spaces. Our reasoning will rely on the identification (17).

2.3. Fictitious domain strategy for particulate flow

In [23] the rigid body motion condition (RBM) in (3) was imposed by means of a fictitious domain strategy, i.e. integrating it into the trial and test space of the according Galerkin FEM and PG-FVM, respectively, defined on the whole domain Ω . The adapted trial space $\mathbf{V}_h^{\text{RBM}}$ was defined by the decomposition

$$\mathbf{V}_h^{\text{RBM}} := \mathbf{V}_h^f \oplus \mathbf{V}_h^{\text{lin}} \oplus \mathbf{V}_h^{\text{rot}} \quad (18)$$

into the usual finite element space $\mathbf{V}_h^f := \text{span}\{\varphi_i \mathbf{e}_k\}_{k=1, \vec{x}_i \in \Omega_f}^d$ for the fluid domain Ω_f and suitable spaces $\mathbf{V}_h^{\text{lin}}, \mathbf{V}_h^{\text{rot}}$ for the linear and angular components of the velocity in P . $\mathbf{V}_h^{\text{lin}}$ and $\mathbf{V}_h^{\text{rot}}$ are constructed by adding up all the degrees of freedom, i.e. shape functions, which lie within P and introducing a rotational component: Definition of the two functions

$$\varphi_{P_h}(\vec{x}) := \sum_{\vec{x}_i \in P} \varphi_i(\vec{x}) \quad \text{and} \quad \varphi_{P_h}^{\mathbf{r}}(\vec{x}) := \sum_{\vec{x}_i \in P} \varphi_i(\vec{x}) \mathbf{r}_i \quad (19)$$

with the piecewise constant approximation \mathbf{r}_i for the radial direction $\mathbf{r}(\vec{x})$ given by

$$\bar{\mathbf{r}}(\vec{x}) := \mathbf{r}_i := \vec{x}_i - \vec{x}_c, \quad \text{for } \vec{x} \in \text{supp}(\varphi_i).$$

and center of mass \vec{x}_c of P yields the following spaces for the translational and rotatinal degrees of freedom of a particle:

$$\mathbf{V}_h^{\text{lin}} := \text{span}\{\varphi_{P_h} \mathbf{e}_k\}_{k=1}^d \quad \text{and} \quad \mathbf{V}_h^{\text{rot}} := \text{span}\{\mathbf{e}_k \times \varphi_{P_h}^{\mathbf{r}}\}_{k=1}^d. \quad (20)$$

We emphasize that their definition is therefore based on the shape functions w.r.t. the underlying unfitted grid \mathcal{T}_h . It was already concluded in [23] that the resulting unfitted scheme causes oscillations of the pressure.
145

3. Analysis of the Origin of Pressure Oscillations

The monolithic scheme for particulate flows derived in [23] is an unfitted scheme, i.e. it does not take the exact location of the immersed boundary ∂P into account. In multiphase flows it is well known that the approximation of the curvature and with it the tension forces localised at the interface is crucial in order to avoid spurious oscillations of the pressure and the velocity. Since the surface forces result in a jump of the pressure at the interface, the reason commonly given for the oscillation is the missing discontinuity of the pressure (see e.g. [16], [21]): Using the standard finite element spaces on the underlying mesh, the non-alignment of the *continuous* finite element space yields a bad approximation of the pressure being discontinuous across the interface. In according XFEM approaches (see e.g. [16], [21], [10], [2], [36]) extended finite element spaces for the pressure aim at capturing the discontinuity.
150
155

We shall follow another reasoning for the derivation of our enriched spaces on the cut elements. Instead of looking at the *value* of the pressure, we focus on the *direction* of forces acting at the interface. In particular, a bad approximation of the shape of the interface implies wrong normals to the interface. Since the pressure acts as force normal to the interface this yields wrong discrete forces. The new perspective of normal vectors suggests to look at *gradients* rather than *values* of the enriching shape functions. The crucial parameter for the construction of the enrichment functions will therefore be the gradient of the shape functions and especially the one of the *test* space.
160
165

3.1. Adjusting the gradient of the test space at the interface

We address the following question: Why does a bad choice of the test space (in the sense of inconsistent gradients) imply wrongly approximated normal forces?

By means of (16) and (17) we can conclude that the choice of unfitted linear finite elements as test space is equivalent to balancing along the boundaries of the associated control volumes. In particular, the discrete representation of the particle is the summation of all barycentric control volumes associated with nodes within the particle, i.e. $P_h := \bigcup_{\vec{x}_i \in P} B_i$ (see red curve in Fig. 3, left). This observation can be derived directly from the summation in (19), see also [23]. The discrete interface along which the forces are acting has the *zig-zag* shape as depicted in Figure 3. Defining suitable parametric mappings $\gamma : [0, 2\pi] \rightarrow \partial P$ and $\gamma_h : [0, 2\pi] \rightarrow \partial P_h$ the following property was proven in [23]:
170
175

$$\gamma'_h(\theta) \not\rightarrow \gamma'(\theta) \quad \text{pointwise for } h \rightarrow 0. \quad (21)$$

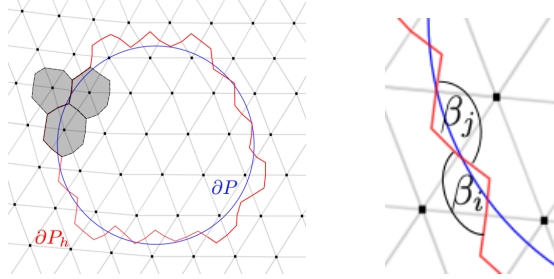


Figure 3: Left: Discrete interface ∂P_h (red line) for the barycenter PG-FVM with $P_h = \bigcup_{\vec{x}_i \in P} B_i$ and three control volumes (shaded grey). Right: Angles β_i, β_j of the zig-zag shape of ∂P_h .

The proof of (21) relies on the observation that the direction of the discrete normals to ∂P_h given by the boundaries of the control volumes deviates by a mean angle of $\beta/2$ (see Fig. 3, right). Therefore, the normal directions will not converge towards the normals of the real interface ∂P .

Beside the identification (17) which refers to the complete stresses, application of (16) in particular yields the following identification of the pressure terms:

$$b_{\text{FE}}(\varphi_i \mathbf{e}_k, \Pi(p)) = b_{\text{FV}}(\Pi(\varphi_i \mathbf{e}_k), p) \quad (22)$$

$$\iff - \int_{\Omega} p \nabla \varphi_i \cdot \mathbf{e}_k \, d\mathbf{x} = \int_{\partial B_i} p \mathbf{n} \cdot \Pi(\varphi_i \mathbf{e}_k) \, d\mathbf{s}, \quad (23)$$

for $\varphi_i \in P^1(\mathcal{T}_h)$, $p \in P^0(\mathcal{T}_h)$ and $0 \leq k \leq d$ (cf. [23]). In other words, testing with $\varphi_i \mathbf{e}_k$ is equivalent to balancing the force exerted by the pressure along ∂B_i . We emphasize that (22) is valid exactly only for an elementwise constant pressure. More effort with suitable error estimates is necessary for general spaces. Since the principal reasoning will not differ it is sufficient for our purposes. In Figure 3 (left) single control volumes involved in the computation are shown shaded in grey.

The equality (23) reveals, that the normal direction \mathbf{n} along ∂B_i inherited in the associated PG-FVM is determined by the gradient $\nabla \varphi_i$ of the Galerkin FE test function. We emphasize this observation with the following remark:

Remark 2 (Relation between normal forces and test space gradients). *Regarding the identification in (23) the normal direction \mathbf{n} of the force exerted by the pressure is directly correlated with the direction of the gradient $\nabla \varphi_i$ of the associated test function.*

We conclude, that due to (21) and (23) the approximation of the local forces will not converge onto the real forces. Therefore, the discrete problem is not consistent with the continuous one and leads to oscillations in the pressure. Figure 12 (d)-(f) shows the oscillating pressure along the interface for the famous cylinder flow benchmark.

In order to define consistent gradients we relocate the DoFs onto the interface and redefine the shape functions as described in the following section.

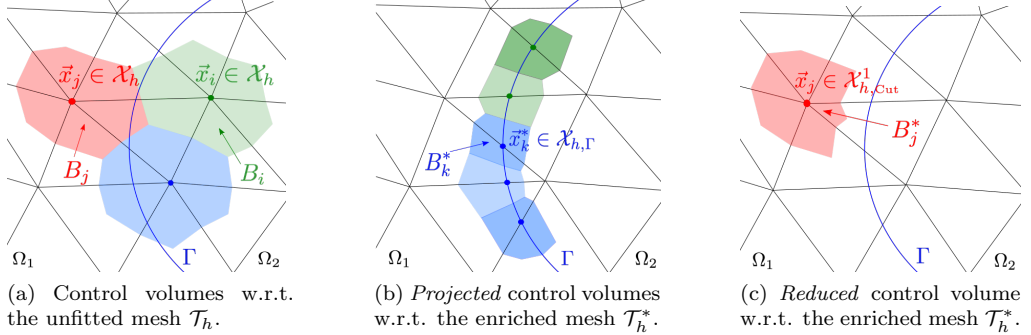


Figure 4: Comparison of the control volumes for the (a) original and the (b),(c) enriched space. The control volumes of the PG-FVM can be interpreted as the test space.

4. Boundary Fitted Scheme for Particulate Flows

Particulate flows can be seen as two-phase flows where the second phase is rigid. As a consequence, the pressure in the rigid phase does not contribute to the dynamics of the whole system and only values of the pressure on ∂P are needed for the computation. Moreover, the velocity in P and on ∂P depends on \mathbf{U} and $\boldsymbol{\omega}$ only. Altogether, the domain occupied by the particle does not need to be treated as a distinct phase and the degrees of freedom in P can be utilized for the discretization in Ω_f . Therefore we will proceed in two steps to define the boundary fitted spaces: We first enrich the finite element spaces on elements which are cut by the interface comparable to the spaces defined by other XFEM approaches. Secondly, we *re-associate* the enriching degrees of freedom to the vertices $\vec{x}_i \in P$ lying inside a particle. As a result, we regain a discretisation with respect to the original grid \mathcal{T}_h . For the sake of generality we denote the interface by Γ (instead of ∂P) and the two subdomains by Ω_1 and Ω_2 (instead of Ω_f and P).

4.1. Locally enriched finite element spaces - flat-top basis for a one-domain problem

Step 1 - Enriching the finite element space on cut elements: For the construction of gradient-consistent enriched spaces we proceed via enriching the test space of the PG-FVM, i.e. we introduce new control volumes: From the perspective of the barycentric PG-FVM and regarding the identification (16) together with the explanations given in the last section, it is reasonable to define the enriching control volumes B_k^* along the interface in order to approximate the normal direction appropriately. As depicted in Figure 4b we construct the control volumes by simply choosing the barycenters of only the cut part of the element. By means of the mapping Π between the according test spaces and $\chi_k^*(\vec{x})|_{B_k^*} \equiv 1$, we get

$$\varphi_k^*(\vec{x}) := \Pi^{-1}(\chi_k^*(\vec{x}))$$

for the enriching test functions φ_k^* of the associated Galerkin FEM. By construction of B_k^* the φ_k^* satisfy the Kronecker-delta property with respect to nodes \vec{x}_k^* on the interface.

We therefore denote the φ_k^* as *projected* shape functions (onto Γ_h). The accordingly adapted shape of the φ_k^* is shown in Figure 6a.

Furthermore, in order for \mathcal{B}_h^* to be still a partition of Ω after adding B_i^* , the control volumes associated with original mesh nodes like B_j in Figure 4a need to be *reduced* to B_j^* as shown in Figure 4c. As a consequence, the test function $\varphi_j^* := \Pi^{-1}(\chi_j^*(\vec{x}))$ satisfies the Kronecker-delta property with respect to the nodes \vec{x}_k^* on the interface as well. We therefore denote the adjusted φ_j^* as *reduced* shape functions (w.r.t. Γ_h). The accordingly adapted shape of the φ_j^* is shown in Figure 7a.

With these considerations, we formally derive the enriched test space as follows: Let \mathcal{X}_h be the set of all vertices of \mathcal{T}_h , $\mathcal{X}_{h,\text{cut}}$ the vertices of all cut elements and $\mathcal{X}_{h,\Gamma} := \bigcup_{T \in \mathcal{T}_h} \partial T \cap \Gamma$ be the set of all intersecting points of Γ with the edges of elements, i.e. $\mathcal{X}_{h,\Gamma} = \{\vec{x}_k^*\}_k$. The (d-1)-dimensional convex hull of all points of $\mathcal{X}_{h,\Gamma}$ yields a piecewise planar approximation Γ_h of Γ . Let further $\Omega_{1,h}$ and $\Omega_{2,h}$ be the corresponding subdomains of Ω satisfying $\partial\Omega_{1,h} \cap \partial\Omega_{2,h} = \Gamma_h$ and $\mathcal{X}_h^1, \mathcal{X}_h^2$ the related set of vertices. We introduce the set of all *cut elements* $\mathcal{T}_{h,\text{cut}} := \{T \in \mathcal{T}_h : T \cap \Gamma \neq \emptyset\}$. By means of $\Omega_{1,h}$ and $\Omega_{2,h}$ all cut elements $T \in \mathcal{T}_{h,\text{cut}}$ can be decomposed into the parts lying on either side of Γ_h , i.e. $\mathcal{T}_{h,\text{cut}}^1 := \{T \cap \Omega_{1,h} : T \in \mathcal{T}_{h,\text{cut}}\}$ and $\mathcal{T}_{h,\text{cut}}^2 := \{T \cap \Omega_{2,h} : T \in \mathcal{T}_{h,\text{cut}}\}$, respectively. Based on the subelements of $\mathcal{T}_{h,\text{cut}}^1$ and $\mathcal{T}_{h,\text{cut}}^2$ we define the new grid

$$\mathcal{T}_h^* := (\mathcal{T}_h \setminus \mathcal{T}_{h,\text{cut}}) \cup \mathcal{T}_{h,\text{cut}}^1 \cup \mathcal{T}_{h,\text{cut}}^2.$$

\mathcal{T}_h^* can be interpreted as a special non-regular refinement of \mathcal{T}_h with respect to Γ .

Furthermore, the set of vertices $\mathcal{X}_{h,\text{cut}}$ can be decomposed into the set $\mathcal{X}_{h,\Gamma}$ of vertices on Γ_h and those being part of \mathcal{X}_h and belonging to either side Ω_j , $j = 1, 2$, of the interface. This yields $\mathcal{X}_{h,\text{cut}} = \mathcal{X}_{h,\Gamma} \cup \mathcal{X}_{h,\text{cut}}^1 \cup \mathcal{X}_{h,\text{cut}}^2$, with *near-interface vertices* $\mathcal{X}_{h,\text{cut}}^j := \{\vec{x} \in \mathcal{X}_{h,\text{cut}} \setminus \mathcal{X}_{h,\Gamma} : \vec{x} \in \Omega_j\}$, $j = 1, 2$. By numbering all vertices of the refined mesh \mathcal{T}_h^* we can assign indices to different subgroups in accordance to the described groups of vertices. Following the notations for the vertices we denote the corresponding set of indices by $\mathcal{I}_h, \mathcal{I}_h^1, \mathcal{I}_h^2, \mathcal{I}_h^*, \mathcal{I}_{h,\text{cut}}, \mathcal{I}_{h,\Gamma}, \mathcal{I}_{h,\text{cut}}^1$ and $\mathcal{I}_{h,\text{cut}}^2$. This yields for example $\mathcal{I}_h \subset \mathcal{I}_h^*$. Based on \mathcal{T}_h^* we define the nodal basis $\{\varphi_i\}_{i \in \mathcal{I}_h^*}$ and the *enriched* finite element space then reads $\mathcal{V}_h^* = \text{span}\{\varphi_i\}_{i \in \mathcal{I}_h^*}$. By construction, the test spaces of the Galerkin FEM and PG-FVM are again related by the bijective map Π and it is

$$\dim(\Pi(\mathcal{V}_h^*)) = \dim(\mathcal{V}_h^*).$$

Finally, we define \mathcal{V}_h^* as the trial function space for both, the Galerkin FEM and the PG-FVM. In particular, we get $\mathcal{V}_h^{f,*} := \text{span}\{\varphi_i\}_{i \in \mathcal{I}_h^1}$ as the finite element space for the fluid domain, containing the reduced shape functions φ_j^* defined on the near-interface vertices $\mathcal{X}_{h,\text{cut}}^1$.

Remark 3 (Enrichment of finite element spaces yields fitted scheme). *Apparently, our definition of the enriched space \mathcal{V}_h^* is nothing else but the usual finite element space w.r.t. the boundary fitted mesh \mathcal{T}_h^* based on an interface-adaptive mesh refinement. We emphasize that it can similarly be interpreted as an enrichment comparable to the extended spaces defined e.g. in [19] of [16]. Instead of re-meshing the whole grid \mathcal{T}_h or moving single grid points $\vec{x}_i \in \mathcal{T}_h$, the finite element space on the cut elements will be enriched by the functions φ_k^* , see Fig. 6a. The enrichment is even comparable to the*

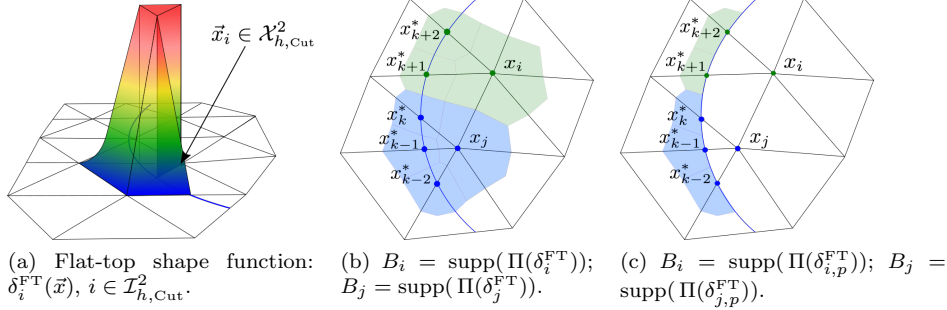


Figure 5: (a) Flat-top shape function; (b) associated control volumes B_i , B_j for the vertices \vec{x}_i , \vec{x}_j of the velocity DoFs in P and (c) of pressure DoFs on Γ . It is $\mathcal{I}_i^{\text{FT}} = \{k-2, k-1, k\}$ and $\mathcal{I}_j^{\text{FT}} = \{k+1, k+2\}$.

enrichment in [19] or [16], but with slightly different shape functions. As we will see in Section 4, our choice provides the consistency of the gradients.

²⁴⁰ **Remark 4 (Non-extended enrichment of finite element spaces).** In contrast to most XFEM approaches the described enrichment does not lead to an extension of the domain across the boundary, since it introduces the degrees of freedom on the interface. In particular, the enriching shape functions satisfy the Kronecker-delta property for the new nodes located on the interface.

It should be noted that $\mathcal{T}_{h,\text{Cut}}^1$ and $\mathcal{T}_{h,\text{Cut}}^2$ will not only consist of triangles or tetrahedrons, but also of quadrilaterals or hexahedrons, prisms and pyramids, respectively (see Section 5.3 for a detailed description of considered elements). As a consequence, for $\mathcal{V}_h = \mathcal{P}^1(\mathcal{T}_h)$ on \mathcal{T}_h the enriched space \mathcal{V}_h^* on \mathcal{T}_h^* will contain not only linear but also multi-linear shape functions.

Step 2 - Re-Association of the enriching degrees of freedom: For the re-association we consider the *near-interface vertices* $\vec{x}_i \in \mathcal{X}_{h,\text{Cut}}^2 (= \mathcal{X}_h \cap P)$ lying on cut elements and in P . Let $T \in \mathcal{T}_{h,\text{Cut}}$ and $(\vec{x}_k^*, \vec{x}_i) = e \subset \partial T$ denote a part of an edge cut by the interface, i.e. $k \in \mathcal{I}_{h,\Gamma}$, $i \in \mathcal{I}_{h,\text{Cut}}^2$. The mapping for the re-association will be formulated via the index set

$$\mathcal{I}_i^{\text{FT}} := \{k \in \mathcal{I}_{h,\Gamma} : (\vec{x}_k^*, \vec{x}_i) = e \subset \partial T, T \in \mathcal{T}_{h,\text{Cut}}\} \quad \forall i \in \mathcal{I}_{h,\text{Cut}}^2, \quad (24)$$

(see Fig. 5b, 5c). Therefore, the set $\mathcal{I}_i^{\text{FT}}$ contains all indices $k \in \mathcal{I}_{h,\Gamma}$ of vertices $\vec{x}_k^* \in \partial P$ which share their edge with the vertex $\vec{x}_i \in P$. As depicted in Figure 5b for two vertices \vec{x}_i , $\vec{x}_j \in P$ it is $|\mathcal{I}_i^{\text{FT}}| = 2$, $|\mathcal{I}_j^{\text{FT}}| = 3$, i.e. it can contain more than one vertex associated to the same vertex of $\mathcal{X}_{h,\text{Cut}}^2$. By means of $\mathcal{I}_i^{\text{FT}}$ we can adjust the enrichment functions φ_i^* for the near-interface vertices $\vec{x}_i \in P$ by simply summing up all enrichment functions associated to \vec{x}_i which yields the shape function

$$\delta_i^{\text{FT}}(\vec{x}) := \varphi_i^*(\vec{x}) + \sum_{k \in \mathcal{I}_i^{\text{FT}}} \varphi_k^*(\vec{x}) \quad \forall i \in \mathcal{I}_{h,\text{Cut}}^2. \quad (25)$$

In the case of $|\mathcal{I}_i^{\text{FT}}| = 2$ it follows directly from the summing up, that the adjusted δ_i^{FT} are constantly 1 on $T \cap P$ and in particular on the edge $\Gamma_h \cap T$ (see Fig. 5a for the two dimensional case). Therefore, we denote the functions δ_i^{FT} as *flat-top* (FT) functions. The locally enriched finite element space for particulate flow finally reads

$$\mathcal{V}_h^{\text{FT},*} := \mathcal{V}_h^{f,*} \oplus \text{span}\{\delta_i^{\text{FT}}\}_{i \in \mathcal{I}_{h,\text{Cut}}^2}.$$

245 **Remark 5 (Flat-Top representation of the solution).** *It should be noted that in the case of $|\mathcal{I}_i^{\text{FT}}| > 1$ the approximation of the solution on the interface is reduced. The flat-top function on a triangle cut by Γ_h as depicted in Figure 5a provides only piecewise constant approximation along the interface $\Gamma_h \cap T$. Furthermore, the control volumes get enlarged (see green and blue volumes in Fig. 5b). However, the global approximation will not be impaired: Due to the summing up of the original shape functions in (25) the solution is approximated by a bi-linear function inside the fluid, see Fig. 5a. Moreover, in the case of the variable \mathbf{U} the local summing up is just in accordance with the construction of the final shape function, see (26).*

255 By means of the remapping we constructed shape functions which are finally defined on the finite elements of the original mesh. We emphasize that the flat-top functions still possess their degrees of freedom exactly on the interface. Inspiration for that choice of shape functions was given by the work on a meshfree method of [38]. In meshfree methods the local approximation space gets multiplied by functions forming a PU. They are supposed to provide locality and global regularity. The purpose of the flat-top function 260 is similarly a localisation by projecting the numerical domain onto the physical domain of the fluid. Regularity was already proven in [23] (see also Section 6).

4.2. Imposing the rigid body motion constraint

So far we enriched the finite element space in order to capture the interface more accurately. The second task is a suitable imposition of the interface conditions (3). Regarding the definition (20) we can easily derive a boundary fitted version of the spaces \mathbf{V}_h^f , $\mathbf{V}_h^{\text{lin}}$ and $\mathbf{V}_h^{\text{rot}}$ based on the enriched space $\mathcal{V}_h^{\text{FT},*}$. Let $\mathcal{I}_{h,P} := \{i \in \mathcal{I}_h : \vec{x}_i \in P, i \notin \mathcal{I}_{h,\text{Cut}}^2\}$ be the index set for vertices lying inside P and *not* near the interface. In analogy to (19) and inheriting the boundary fitted spaces, we define

$$\varphi_{P_h}^{\text{FT}}(\vec{x}) := \sum_{i \in \mathcal{I}_{h,\text{Cut}}^2} \delta_i^{\text{FT}}(\vec{x}) + \sum_{i \in \mathcal{I}_{h,P}} \varphi_i(\vec{x}), \quad (26)$$

$$\varphi_{P_h}^{\text{FT,r}}(\vec{x}) := \sum_{i \in \mathcal{I}_{h,\text{Cut}}^2} \delta_i^{\text{FT}}(\vec{x}) \mathbf{r}_i + \sum_{i \in \mathcal{I}_{h,P}} \varphi_i(\vec{x}) \mathbf{r}_i. \quad (27)$$

This yields

$$\mathbf{V}_h^{\text{RBM},*} := \mathbf{V}_h^{f,*} \oplus \mathbf{V}_h^{\text{FT,lin}} \oplus \mathbf{V}_h^{\text{FT,rot}}$$

265 with $\mathbf{V}_h^{\text{FT,lin}} := \text{span}\{\varphi_{P_h}^{\text{FT}} \mathbf{e}_k\}_{k=1}^d$, $\mathbf{V}_h^{\text{FT,rot}} := \text{span}\{\mathbf{e}_k \times \varphi_{P_h}^{\text{FT,r}}\}_{k=1}^d$ and velocity space for the fluid $\mathbf{V}_h^{f,*} := \text{span}\{\varphi_i^* \mathbf{e}_k\}_{k=1, i \in \mathcal{I}_h^1}^d$ which compared to \mathbf{V}_h^f in (18) espacially contains the reduced shape functions near the interface.

The pressure space contains the flat-top functions for the degrees of freedom on the interface as well. They need to be reduced to the fluid domain by $\delta_{i,p}^{\text{FT}}|_{\Omega_{h,1}} := \delta_i^{\text{FT}}$ and $\delta_{i,p}^{\text{FT}} = 0$, else, which yields

$$\mathcal{P}_h^{\text{RBM},*} := \mathcal{V}_h^{f,*} \oplus \text{span}\{\delta_{i,p}^{\text{FT}}\}_{i \in \mathcal{I}_{h,\text{Cut}}^2}.$$

By means of the mapping $\Pi : \mathcal{V}_h^* \rightarrow \overline{\mathcal{V}_h^*}$ the test spaces for the associated PG-FVM can be defined accordingly. We emphasize that due to the definition of $\delta_{i,p}^{\text{FT}}$ the related control volumes of the pressure variables on the interface only lie inside $\Omega_{h,1}$. Figure 5c illustrates the according control volumes (being additionally enlarged along the interface due to the summation).

4.3. Numerical scheme - discretisation in time

For the discretisation of the time derivative an implicit Euler scheme is applied. The particles are modeled in a Lagrangian frame and the new location of the particles and the interface needs to be updated after each time step. The immersed boundary strategy in Section 2 was derived for a stationary interface. For a moving interface the solution is in general not continuous in time. A potential problem can arise if nodes within a particle will be part of the fluid grid in the next time step, also called *freed nodes*. Some discretisations combining a sharp interface representation with a Eulerian grid suffer from oscillations in the solution due to that discontinuity, cf. [43], [6], [51], [42], [26]. Our scheme does not additionally account for that circumstance and interpolates the solution in *freed nodes* based on the trial space. Oscillations were only observed on coarse meshes and were damped fast under refinement, see Section 7.1. Regarding our numerical results this implementation near the interface is sufficient and did not have negative impact to the global discretisation error. For higher Reynolds numbers and deformable interfaces this strategy presumably needs to be adapted.

4.4. Numerical scheme - discretisation in space

We begin with the unconstraint Navier-Stokes equations defined on the whole domain Ω . Let

$$\mathbf{M}^* [\mathbf{u}, p]^T = \mathbf{f}$$

be the unconstraint linear system w.r.t. the adaptively refined mesh \mathcal{T}_h^* , i.e. $\mathbf{M}^* \in \mathbb{R}^{M \times M}$ and $M := (d+1)N$, $N := \dim(\mathcal{V}_h^*)$. Since the adapted spaces $\mathbf{V}_h^{\text{RBM},*}$ and $\mathcal{P}_h^{\text{RBM},*}$ were derived from the standard shape functions of the enriched space \mathcal{V}_h^* , the boundary fitted scheme for particulate flows will be formulated in the following subsections as some transformation of \mathbf{M}^* .

4.4.1. RBM-Projection

In [23] the transformations were derived being necessary for the decomposition of the adapted space $\mathbf{V}_h^{\text{RBM}}$ into $\mathbf{V}_h^{\text{lin}}$ and $\mathbf{V}_h^{\text{rot}}$. The unconstraint velocity field gets projected onto a rigid body motion in P . For a detailed description we refer to [23]. Analogue transformations can be applied in case of $\mathbf{V}_h^{\text{RBM},*}$ inheriting the discrete delta functions δ_j^{FT} on ∂P , see (26), (27). We denote the resulting system by $\mathbf{M}_{\text{RBM}}^*$.

4.4.2. Flat-Top-Mapping

For the velocity degrees of freedom the remapping from Lagrangian to Eulerian grid points according to (24) is already inherited in the global summations due to (26), (27). For the remapping of the pressure degrees of freedom simply a global projection matrix \mathbf{P} satisfying $\mathbf{P}[k][i] = 1$ for all $i \in \mathcal{I}_{h,\text{cut}}^2$ and $k \in \mathcal{I}_i^{\text{FT}}$ needs to be applied as a post processing on \mathbf{M}^* . The discrete system for particulate flow finally reads

$$\mathbf{M}_{\text{RBM}}^{\text{FT},*} = \mathbf{P}^T \mathbf{M}_{\text{RBM}}^* \mathbf{P}.$$

4.5. Implementation details

The proposed enriched space $\mathcal{P}^1(\mathcal{T}_h^*)$ essentially forms the function space w.r.t. an interface adapted mesh \mathcal{T}^* . We emphasize however, that in analogy to other extended finite element approaches, to avoid impaired efficiency we do not refine the mesh, but adapt the discrete scheme locally. The assembling of the discrete system can be performed w.r.t. the non-cut elements in two steps and based on standard algorithms as follows:

Step 1 - Standard assembling on cut reference elements: Algorithms for finite element schemes on unstructured meshes usually exploit the possibility to map each (unstructured) element of the mesh onto its reference element. The assembling of the discrete system therefore depends simply on the coordinates of the corners of an element. As a consequence, on each cut element $T \in \mathcal{T}_{h,\text{cut}}$ the same standard routines for unstructured elements can be applied for each cut part of the original element. This simply requires calling these routines twice and with respect to the corresponding new coordinates. Moreover, we maintain local stencils and optimal convergence properties as will be illustrated by the numerical results. Furthermore, we can assume that for the sub-elements the discretisation on the reference element is well defined, see Section 6.3. Of course, the resulting number of local equations is increased by the number of new enriching functions.

Step 2 - Re-mapping onto original DoFs: Due to the re-association in (24) the re-mapping of the enriching DoFs onto the DoFs of the vertices of the original mesh is simply done by summing them up.

5. Properties of the Enriched Space

In contrast to other immersed boundary methods, where the enriching functions are commonly chosen w.r.t. the original mesh, the function space $\mathcal{P}^1(\mathcal{T}_h^*)$ is chosen w.r.t. the mesh *including* nodes on the interface. The direct consequence is the Kronecker-delta property of the shape functions w.r.t. the interface and its implications will be explained in Section 5.2. First, we mention a further important property:

5.1. Partition of Unity

By construction, the enriched spaces again form a partition of unity. The following remark emphasizes the importance of this property:

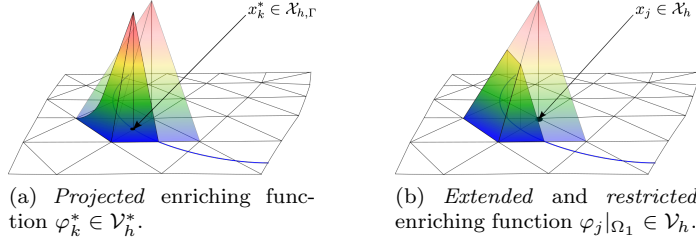


Figure 6: Projection of the enriching function φ_k^* yields a *shifted* gradient. This shift is particularly relevant for the *test space*.

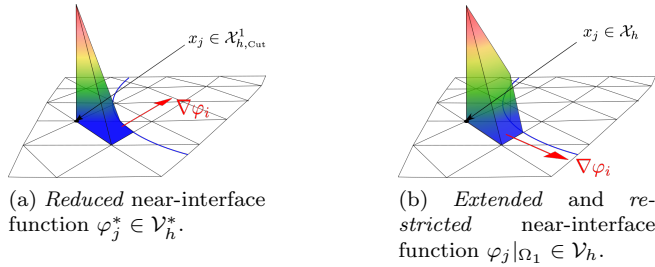


Figure 7: Reduction of the near-interface function φ_j^* yields a *shifted* gradient. This shift is particularly relevant for the *trial space*.

Remark 6 (Partition of Unity). *The PU property*

$$\sum_{i \in \mathcal{I}_h^*} \varphi_i(\vec{x}) = 1 \quad \forall \vec{x} \in \Omega$$

is a necessary and sufficient condition to guarantee mass conservation, see e.g. [28]. The standard finite element shape functions defined on the original mesh T_h satisfy the PU property. After the introduction of the shape functions in the projected nodes the reduction step becomes necessary in order to preserve the PU property.

5.2. The Kronecker-delta property: Consistency of the gradients

The request for the Kronecker-delta property of the enriching shape functions w.r.t. the interface together with the PU property has two implications for the gradients of both the enriching and the near-interface shape functions:

³⁴⁰ 5.2.1. *Projection instead of Extension: Consistency of the gradients of the test space*

Using the shape functions w.r.t. the original mesh is often described as an *extension* of the domain across the interface (see e.g. [19]). On the continuously extended domain the common finite element analysis based on the standard spaces of the original mesh can be applied. However, the direction of the gradient will remain unchanged independently

³⁴⁵ of the location of the interface. In contrast to that, the *projection* onto the interface due to $\varphi_k^*(\vec{x}_i) = \delta_{ki}$ yields a *shift* of the gradient. The comparison is depicted in Figure 6. By means of the the mapping Π and association with the PG-FVM we argued in Section 4.1 that this shifting leads to *consistent gradients of the test space* in the sense of consistent normal forces.

³⁵⁰ 5.2.2. *Reduction instead of Restriction: Consistency of the gradients of the trial space*

In order to satisfy the PU property for the whole enriched space, the projection of the enriching shape function requires that the shape functions φ_j associated with near-interface vertices $\vec{x}_j \in \Omega_f$ be adapted as well. This *adaptation* was denoted by *reduction* of yielding the shape funcitons to satisfy the Kronecker-delta property w.r.t. the interface as well. That results in *consistent gradients of the solution space* in the following sense: For all $\vec{x}_j \in \mathcal{X}_{h,\text{Cut}}^1$, it is

$$\varphi_j^*(\vec{x})|_{\Gamma_h} \equiv 0 \quad \Rightarrow \quad \nabla \varphi_j^* \parallel \mathbf{n}_h,$$

³⁵⁵ with normal direction \mathbf{n}_h with respect to Γ_h . As a consequence, the gradients of the degrees of freedom *off* the interface are directed normal to the interface (see Fig. 7a). This is consistent with the physical reality that only the normal components of forces matter for the interface dynamics. Figure 7a again illustrates the *shifting* of the gradient of a reduced shape function φ_j^* associated to a vertex $\vec{x}_j \in \mathcal{X}_{h,\text{Cut}}^1$ in comparison to the original shape function φ_j .

³⁶⁰ **Remark 7 (Pressure oscillation in particulate flows).** *Previous to the development of the proposed enrichment scheme another approach was implemented following a ghost fluid technique. This approach could only provide a better approximation to the values at the interface without taking the gradients into account. Accordingly, the oscillations could not be reduced. In contrast, the enrichment strategy implies correct normals at the interface (see Fig. 7a). The numerical tests in Section 7.1 show that the derived enriched spaces lead to the elimination of the oscillations and therefore confirm the above argumentation. This result is in accordance with the observations reported in [12]. Herein it was shown, that it is crucial to compute the curvature precisely in order to avoid parasitic currents.*

5.3. *Existence of a local finite element space on cut elements*

³⁷⁰ A common problem of most cut element methods is the handling of the different variants of how an element $T \in \mathcal{T}_h$ can be cut into two elements, cf. [33], [9]. Most approaches aim to preserve the discrete scheme for the original nodes. You can either employ a non-local interpolation strategy or reduce the number of local unknowns. In fictitious domain methods, cf. [15], [1], [44], and similarly for ghost fluid methods, cf. [11], the number of unknowns on the interface coincides with the number of unknowns on T of the original grid. The solution space gets extended onto the whole element T across the interface. The main drawback is potential unphysical behaviour of the solution since values outside the physical domain contribute to the dynamics of the system: In some XFEM methods numerical fluxes across the boundary arise as an artifact of the extension, cf. [27]. The main motivation for choosing the original space is of course that standard discretisation can be applied. Besides that, the extended and restricted shape functions share their good properties with those defined on the whole element.

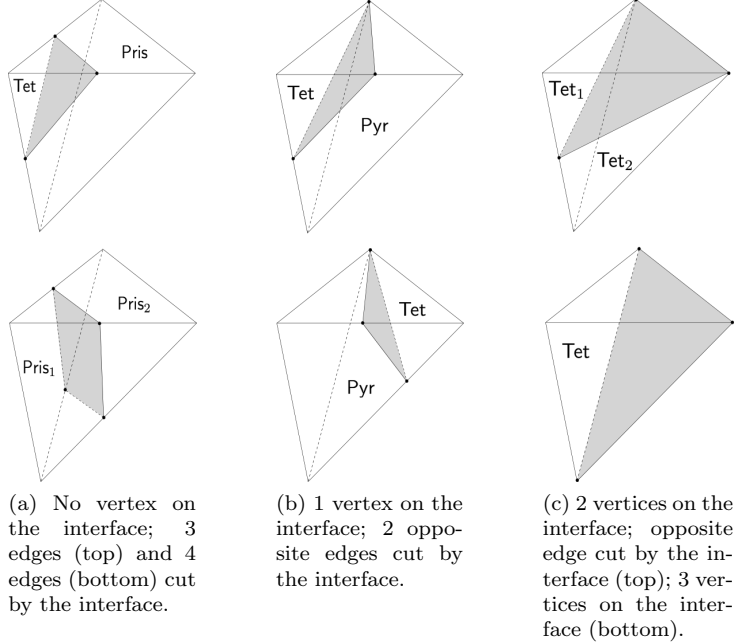


Figure 8: Different cut elements for $d = 3$: (a)-(c) Categorization by the number of vertices and edges cut by the immersed interface.

Our approach of projection and reduction assures optimal and stable local approximation properties as will be shown in Section 6. Appropriate nodal shape functions for $\vec{x}_k^* \in \mathcal{X}_{h,\Gamma}$ with its support on the elements $T \in \mathcal{T}_{h,\text{cut}}^j$, $j = 1, 2$, need to be provided. For piecewise linear finite element spaces $\mathcal{V}_h := \mathcal{P}^1(\mathcal{T}_h)$ on simplicial triangulations suitable local spaces can be defined quite easily: In two dimensions the simplex is a triangle which gets cut into two triangles or a triangle and a quadrilateral on which a linear and bi-linear ansatz exists. In three dimensions the simplex is a tetrahedron and gets cut into combinations of tetrahedra, prisms and pyramids, see Fig. 8. For all these elements local shape functions of second order exist. The details on the local spaces used for our computations can be found in [45]. Our approach certainly will afford more effort for the definition of suitable local spaces on the cut elements, if the mesh contains also quadrilaterals or octahedrons in two or three dimensions, respectively. For all considered applications the simplicial grid was appropriate.

6. Numerical Analysis

In this section we will derive theoretical results for the Galerkin FEM (7), (8) based on the enriched space $\mathbf{V}_h^{\text{RBM},*}$. Inf-sup stability was already proven in [23] for the unfitted space $\mathbf{V}_h^{\text{RBM}}$ in (18). The proof can be similarly applied to $\mathbf{V}_h^{\text{RBM},*}$ based on the enriched mesh \mathcal{T}_h^* .

Unfortunately, due to $R(h) \neq 0$ in (17) for \mathcal{V}_h^* containing multi-linear elements, the theoretical results for the FEM can not directly be transferred to the PG-FVM (11), (12). However, since the enriched mesh \mathcal{T}_h^* contains only a few multi-linear elements along the interface compared to the global number of elements, it is reasonable to assume that $R(h) = O(h^2)$ also holds for the associated PG-FVM. Therefore, we can at least state that the results derived in the following subsections (based on finite element theory together with the identification (16)) at least allow us to expect a similar convergence behaviour for the PG-FVM. As we will see in Section 7 the numerical results for the PG-FVM confirm our reasoning.

6.1. Conditioning

In the case of a moving interface the distance between nodes and the interface can theoretically become infinitely small. Due to the projection and reduction step the finite element spaces are defined with respect to cut elements. Consequently, the shape-regularity of the mesh \mathcal{T}_h^* is not guaranteed (i.e. the existence of a constant $\kappa > 0$ independent of the location of the interface, s.t. $h_T/\rho_T \leq \kappa$, with h_T and ρ_T being the circumcenter and incircle-radius of an arbitrary $T \in \mathcal{T}_h^*$). That is a potential source of ill-conditioning of our discrete scheme. In order to preserve shape-regularity we simply re-define those points $\vec{x}_k^* \in \mathcal{X}_{h,\Gamma}$ whose distance to a point on the Eulerian mesh falls below a certain threshold. To formulate a suitable criterion for a re-definition we choose a lower bound $D > 0$ satisfying $D < h_{\min}$, with $h_{\min} := \min\{h_T : T \in \mathcal{T}_h\}$ being the minimal circumcenter in the original grid. The re-definition then reads:

$$\forall k \in \mathcal{I}_{h,\Gamma} : \text{If } d_{i,k} := |\vec{x}_i - \vec{x}_k^*| \leq D \text{ for any } \vec{x}_i \in \mathcal{T}_h, \text{ then re-define } \vec{x}_k^* := \vec{x}_i. \quad (28)$$

The adapted triangulation \mathcal{T}_h^* satisfies the condition $h_T/\kappa \leq \rho_T$. The proof can be found in [22]. The resulting discrete interface Γ_h approximates Γ less accurate. However, for the choice of $D := h^2 < h_{\min}$, with h being the mean circumcenter of the given grid, we can conclude that the resulting piecewise planar interface Γ_h satisfies

$$\text{dist}(\Gamma_h, \Gamma) \leq c h^2.$$

In a later work we will show that the corresponding discrete scheme maintains optimal approximation order. A higher condition number in favor of a stable solution process for the linear system appears to be a valid strategy confirmed by the numerical simulations in Section 7.

In common XFEM approaches the ill-conditioning of the discrete system is similarly an issue. But in contrast to the shape-regularity above, already small but shape-regular cut elements are critical, since the small support combined with shape functions defined on the original mesh result in an almost-dependency between the enriched degrees of freedom. We emphasize that our projected and reduced shape functions (i.e. in particular not defined w.r.t. the original mesh) possess steeper gradients, which yields a natural stabilisation on very small cut elements:

420 Remark 8 (Natural stabilisation on small cut elements). *The crucial role of the gradient of the projected and restricted shape functions was explained in Sections 5.2.1 and 5.2.2. Besides that, it provides a natural stabilisation and therefore small cut elements do not cause conditioning problems: For linear finite elements it is $|\nabla \varphi_i|_T = 1/h_i$*

(with h_i being the height of T w.r.t. \vec{x}_i and the opposite edge) and therefore they scale inversely proportional to the area of the element.

The Hansbo-averageing is a strategy to handle the issue of ill-conditioning due to small support and other XFEM spaces. We want to mention it in order to contrast it to the proposed re-definition in (28):

Remark 9 (Hansbo-averageing). Formulations based on Nitsche's method [32] introduce an averaging operator $\{\cdot\}$ to re-weight the shape functions on the cut elements by

$$\{\varphi\} := (\kappa_1 \varphi_1 + \kappa_2 \varphi_2)|_{\Gamma}, \quad \varphi_j \in R_j(\mathcal{V}_h), \quad (29)$$

with weights κ_1 and κ_2 satisfying $\kappa_1 + \kappa_2 = 1$ in order to preserve consistency of the discrete scheme. For $T_j := \text{supp}(\varphi_j) \cap T$, $j = 1, 2$, the so called Hansbo-averaging, cf. [19], defines $\kappa_j := T_j/T$. Hence, the weights depend on the size of the relative area of each sub-element which resembles the parameter $d_{i,j}$ in (28). Other weighting strategies are defined in [21], [35], [49] likewise depending on the properties of the sub-elements.

Remark 10 (Neglection vs. Redefinition). A weighting rule which defines $\kappa_1 := 0$ and $\kappa_2 := 1$ in (29) in the case of very small support, i.e. $T_1/T \approx 0$, corresponds to neglecting the presence of the interface on the cut element T . Optimal approximation of the solution can be preserved if a criterion for neglecting is defined suitably, cf. [35]. We however emphasize that the described re-definition in (28) resembles the strategy of neglecting but does not correspond to it: Consider the case of a two-dimensional triangle cut by the interface in such a way that after application of criterion (28) the whole triangle lies on one side of the interface. Therefore, the triangle will not be part of the enrichment. In contrast to neglecting the interface, the re-definition of the node leads to a slight displacement of the interface. In particular, also on the neighbouring elements the shape of Γ_h gets displaced. The essential consequence is the continuity of the interface across neighbouring cut elements.

6.2. Coercivity

The coercivity of $a_{FE}(\cdot, \cdot)$ on $\mathbf{V}_h^{\text{RBM},*}$ directly follows from the coercivity of the continuous bilinear form. This directly implies the important advantage of our approach that no additional stabilisation is needed which can cause numerical fluxes across the interface.

Remark 11 (Coercivity of $a_{FV}(\cdot, \cdot)$). Due to (17) the coercivity of the associated PG-FVM is potentially impaired only on the multi-linear elements. Based on our assumption that $R(h) = O(h^2)$ there exists a $h_{FV} > 0$ and an according constant $C(h_{FV})$ such that the coercivity is satisfied with constant $C(h_{FV})$ and for all $h \leq h_{FV}$.

6.3. Error analysis

A detailed error analysis for the enriched space will be presented in a later work where we consider the simpler problem of an elliptic equation with discontinuous coefficients. Therein we prove optimal convergence of the scheme. Since for stationary Stokes flow the operator is elliptic as well, we can at least partly refer to these results at this point. The convergence results provided by our numerical tests in Section 7.1 provide an experimental validation.

7. Numerical Simulations

In this section we will present the numerical results. For the solution of the non-linear Navier-Stokes equations a **fixed** point iteration is used. For more details we refer to [31].
 465 The arising linear systems have been solved with a geometric multigrid solver provided within the software framework *UG4*, [45], using ILU as smoother and a BiCGSTAB solver for the solution on the coarsest grid.

7.1. Convergence study - flow around a fixed cylinder

In accordance with the numerical studies in [23] we will first evaluate the performance
 470 of the derived scheme by studying its convergence properties. In [23] the convergence rates were impaired by the non-sharp scheme for the interface. The following computations show the improvement provided by the enriched spaces $\mathbf{V}_h^{\text{RBM},*}$ and that the observed rates are optimal.

As in [23] we consider the well known benchmark of flow in a channel around a fixed cylinder as extensively studied by Schäfer and Turek [37]. For the two dimensional case a circle with radius $r = 0.05m$ and center at $(0.2m, 0.2m)$ is placed in a channel with dimensions $H \times L = 2.2m \times 0.41m$. Dirichlet boundary conditions are given on the left and right parts of the outer boundary with a parabolic profile given by

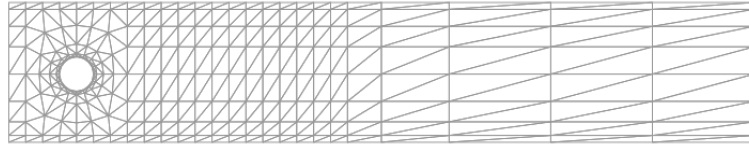
$$u(0, y) = \frac{4y(H-y)}{H^2} U_m, \quad U_m = 0.3 \frac{m}{s}, \quad v(0, y) \equiv 0.$$

On the upper and lower parts of the outer boundary usual no-slip conditions are applied.
 475 The prescribed velocity profile yields the mean velocity $\bar{U} = \frac{2}{3} u(0, \frac{H}{2}) = 0.2 \frac{m}{s}$. For viscosity $\mu = 0.001 \frac{m^2}{s}$ the Reynolds number of the fluid is $Re = \frac{2r\bar{U}}{\nu} = 20$.

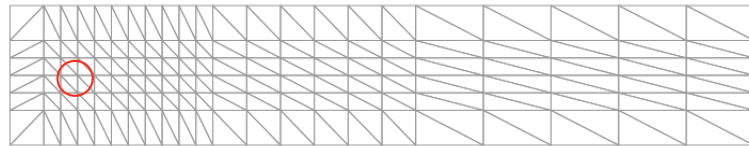
The computations were conducted on the mesh as shown in Fig. 9b. The red line indicates the immersed interface. Due to the setting of the benchmark the motion of the particle is prescribed to zero, i.e. $\mathbf{U} = \boldsymbol{\omega} = \mathbf{0}$. Furthermore, we used the body fitted
 480 mesh of Fig. 9a for comparison of our results with reference computations of an exact interface representation. Plots of the computed velocity and pressure field for the fitted and immersed case are shown in Fig. 10a, 10b and Fig. 11a, 11b, respectively.

7.1.1. Grid convergence

The rates of convergence were computed in the usual L_2 -norm by applying five regular
 485 grid refinements and comparing the solution computed on each grid with the solution on the next finer grid. Since the convergence is commonly impaired by non-linear effects the computations were additionally performed for the linear Stokes equations and identical fluid parameter. The results for the convergence rates for the linear and non-linear test cases are summarized in Tables 1 and 2. In the linear case the rates on the boundary fitted
 490 mesh show order two for the velocity and order one for the pressure for the linear case. This is in accordance with the investigations carried out in [31] for the stabilized finite volume scheme applied here. We measured comparable rates for velocity and pressure for our enriched scheme and the linear case, see Table 1b. That proves the optimal order also numerically. The convergence rates of the scheme without enrichment measured
 495 in [23] are presented in Table 1c. In the linear case they show the reduced rates lying around 1.5 for the velocity and showing more irregular behaviour for the pressure.

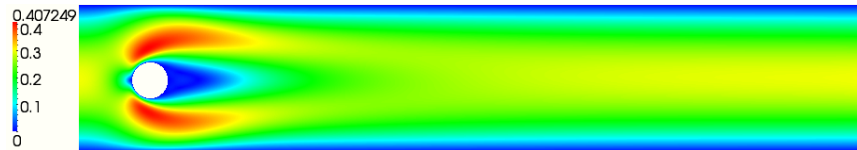


(a) boundary fitted mesh.

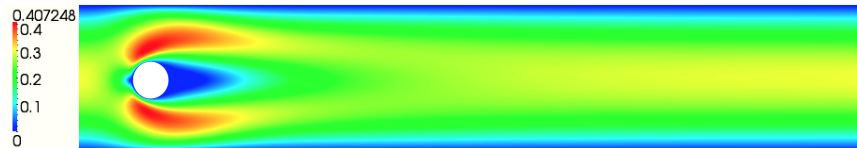


(b) unfitted mesh and immersed interface ∂P (red)

Figure 9: Flow around a fixed cylinder: (a) boundary fitted mesh; (b) unfitted mesh.



(a) Magnitude of the velocity (color) for the boundary fitted mesh in Fig. 9a.



(b) Magnitude of the velocity (color) for the enriched scheme and the unfitted mesh in Fig. 9b.

Figure 10: Magnitude of the velocity (color): (a) boundary fitted mesh; (b) unfitted mesh.

For the non-linear case all three schemes show an irregular behaviour for the velocity rates. This can be traced back to the applied skewed upwind scheme for the convective terms. Similarly in all cases the rates for the pressure behave less regular. A possible reason for that can be the changing representation of the interface on the different grid refinements.



(a) Pressure (color) for the boundary fitted mesh in Fig. 9a.



(b) Pressure (color) for the enriched scheme and the unfitted mesh in Fig. 9b.

Figure 11: Pressure (color): (a) the boundary fitted mesh; (b) the unfitted mesh.

7.1.2. Oscillation of the pressure

Fig. 12 (a)-(c) shows plots of the pressure values along the interface. For comparison Fig. 12 (d)-(f) shows the results of [23] for the scheme without enrichment. The oscillations could successfully be eliminated. We emphasize that for the non-sharp computations the oscillation did not vanish under grid refinement and their frequency even increases. This observation was assigned in [23] to a local origin of the error on each element. With regard to Remark 7 the proposed enrichment leads to an elementwise local correction.

In order to further investigate the quality of the pressure solution the difference

$$\Delta p(x, y) := p(0.15, 0.2) - p(0.25, 0.2) \quad (30)$$

between the front and back point of the interface was evaluated. A comparison with the reference [24] and with the according results in [23] without enrichment is shown in Table 3.

7.2. Validation of the translational component - sedimenting particle

For the validation of the translational component \mathbf{U} of a particle we conducted the test problem of a sedimenting particle falling (infinitely long) under gravity in a channel of width D . The problem was already examined in [23]. The computed stationary (long term) solution is the terminal velocity $\mathbf{U}(r) = (0, U_{\text{term}}(r))^T$ which the particle reaches in its equilibrium between friction and gravitational acceleration. Because of the finite width D of the channel an additional so called *wall-force* F_w acts on the particle. Since F_w depends on the relation $\frac{2r}{D}$ (*blockage ratio*) the terminal velocity $U_{\text{term}}(r)$ will depend on r and D as well. There exist different asymptotic solutions for the wall force F_w in

l	# DoFs	h_l	$\ u\ _2$	r_l	$\ v\ _2$	r_l	$\ p\ _2$	r_l
1	3,222	1.55e-01	5.36e-03	—	1.13e-03	—	6.88e-04	—
2	12,396	7.76e-02	1.40e-03	1.933	3.03e-04	1.899	2.50e-04	1.460
3	48,600	3.88e-02	3.56e-04	1.978	7.83e-05	1.952	9.77e-05	1.355
4	192,432	1.94e-02	8.95e-05	1.992	1.99e-05	1.977	4.14e-05	1.240
5	765,792	9.70e-03	2.24e-05	1.997	5.01e-06	1.989	1.91e-05	1.118
6	3,055,296	4.85e-03	—	—	—	—	—	—

(a) Convergence rates for the boundary fitted mesh in Fig. 9a.

l	# DoFs	h_l	$\ u\ _2$	r_l	$\ v\ _2$	r_l	$\ p\ _2$	r_l
1	1,755	1.12e-01	7.35e-03	—	3.22e-03	—	6.78e-04	—
2	6,675	5.62e-02	1.85e-03	1.989	8.30e-04	1.954	2.54e-04	1.415
3	26,019	2.81e-02	4.59e-04	2.011	2.10e-04	1.980	1.10e-04	1.212
4	102,723	1.40e-02	1.15e-04	2.003	5.38e-05	1.968	5.12e-05	1.099
5	408,195	7.02e-03	2.86e-05	2.003	1.36e-05	1.983	2.48e-05	1.049
6	1,627,395	3.51e-03	—	—	—	—	—	—

(b) Convergence rates for the unfitted mesh in Fig. 9b with enrichment.

l	# DoFs	h_l	$\ u\ _2$	r_l	$\ v\ _2$	r_l	$\ p\ _2$	r_l
1	1,755	1.12e-01	1.06e-02	—	5.43e-03	—	1.42e-03	—
2	6,675	5.62e-02	3.62e-03	1.545	1.97e-03	1.436	5.55e-04	1.355
3	26,019	2.81e-02	1.49e-03	1.281	7.99e-04	1.306	2.70e-04	1.037
4	102,723	1.40e-02	5.75e-04	1.375	3.27e-04	1.290	1.11e-04	1.288
5	408,195	7.02e-03	2.51e-04	1.193	1.35e-04	1.272	5.60e-05	0.982
6	1,627,395	3.51e-03	—	—	—	—	—	—

(c) Convergence rates for the unfitted mesh in Fig. 9b without enrichment.

Table 1: Grid convergence for the linear flow problem around a fixed cylinder: (a) boundary fitted mesh; (b) unfitted mesh with enrichment; (c) unfitted mesh without enrichment.

the literature. For the case of a two dimensional channel we choose

$$\begin{aligned} F_w(2r, D) &:= -\ln\left(\frac{2r}{D}\right) - 0.9157 + 1.7244\left(\frac{2r}{D}\right)^2 - 1.7302\left(\frac{2r}{D}\right)^4 + O\left(\left(\frac{2r}{D}\right)^6\right), \\ U_{\text{term}}(r) &:= \frac{(\rho_P - \rho_f) g r^2}{4\mu} F_w(2r, D), \end{aligned} \quad (31)$$

as asymptotic solution, see [47], with gravitational acceleration g , density of the particle ρ_P and the density and viscosity of the fluid ρ_f and μ . For fixed channel width the validated value $U_{\text{term}}(r)$ only depends on the radius.

The numerical tests were conducted on an unstructured mesh with dimensions $H \times L = 2 \times 6$. Simple no-slip Dirichlet conditions on the outer boundary are applied. We tested the quality of the approximation by varying the radius r of the particle between 0.02 and 0.55. The results for different levels of refinement are plotted in Fig. 13. For

l	# DoFs	h_l	$\ u\ _2$	r_l	$\ v\ _2$	r_l	$\ p\ _2$	r_l
1	3,222	1.55e-01	2.15e-03	—	6.85e-04	—	3.90e-04	—
2	12,396	7.76e-02	6.57e-04	1.713	2.00e-04	1.776	1.67e-04	1.228
3	48,600	3.88e-02	2.07e-04	1.663	7.98e-05	1.362	1.10e-04	0.605
4	192,432	1.94e-02	6.38e-05	1.702	3.51e-05	1.184	5.41e-05	1.019
5	765,792	9.70e-03	1.85e-05	1.782	1.28e-05	1.462	2.25e-05	1.264
6	3,055,296	4.85e-03	—	—	—	—	—	—

(a) Convergence rates for the boundary fitted mesh in Fig. 9a.

l	# DoFs	h_l	$\ u\ _2$	r_l	$\ v\ _2$	r_l	$\ p\ _2$	r_l
1	1,755	1.12e-01	6.88e-03	—	4.11e-03	—	2.61e-03	—
2	6,675	5.62e-02	3.35e-03	1.039	1.80e-03	1.192	1.09e-03	1.263
3	26,019	2.81e-02	6.21e-04	2.430	3.73e-04	2.270	1.88e-04	2.530
4	102,723	1.40e-02	1.42e-04	2.129	9.33e-05	2.000	5.38e-05	1.805
5	408,195	7.02e-03	3.59e-05	1.982	2.47e-05	1.920	2.38e-05	1.175
6	1,627,395	3.51e-03	—	—	—	—	—	—

(b) Convergence rates for the unfitted mesh in Fig. 9b with enrichment.

l	# DoFs	h_l	$\ u\ _2$	r_l	$\ v\ _2$	r_l	$\ p\ _2$	r_l
1	1,755	1.12e-01	1.40e-02	—	6.66e-03	—	2.85e-03	—
2	6,675	5.62e-02	4.18e-03	1.741	3.29e-03	1.019	1.39e-03	1.032
3	26,019	2.81e-02	1.59e-03	1.395	1.29e-03	1.347	5.12e-04	1.443
4	102,723	1.40e-02	6.34e-04	1.326	5.42e-04	1.254	2.06e-04	1.311
5	408,195	7.02e-03	2.88e-04	1.136	2.16e-04	1.330	8.45e-05	1.287
6	1,627,395	3.51e-03	—	—	—	—	—	—

(c) Convergence rates for the unfitted mesh in Fig. 9b without enrichment

Table 2: Grid convergence for the non-linear flow problem around a fixed cylinder: (a) boundary fitted mesh; (b) unfitted mesh with enrichment; (c) unfitted mesh without enrichment

radii ≤ 0.3 the computed solution of the terminal velocity is in good agreement with the

l	Δp fitted	Δp unfitted + enr	Δp unfitted
1	1.1718e-01	9.9221e-02	7.1641e-02
2	1.1702e-01	1.0593e-01	1.0160e-01
3	1.1724e-01	1.1327e-01	1.0873e-01
4	1.1735e-01	1.1541e-01	1.1238e-01
5	1.1742e-01	1.1652e-01	1.1441e-01
6	1.1747e-01	1.1705e-01	1.1574e-01
Reference		1.1752e-01	

Table 3: Pressure difference Δp as in (30); reference values, cf. [24].

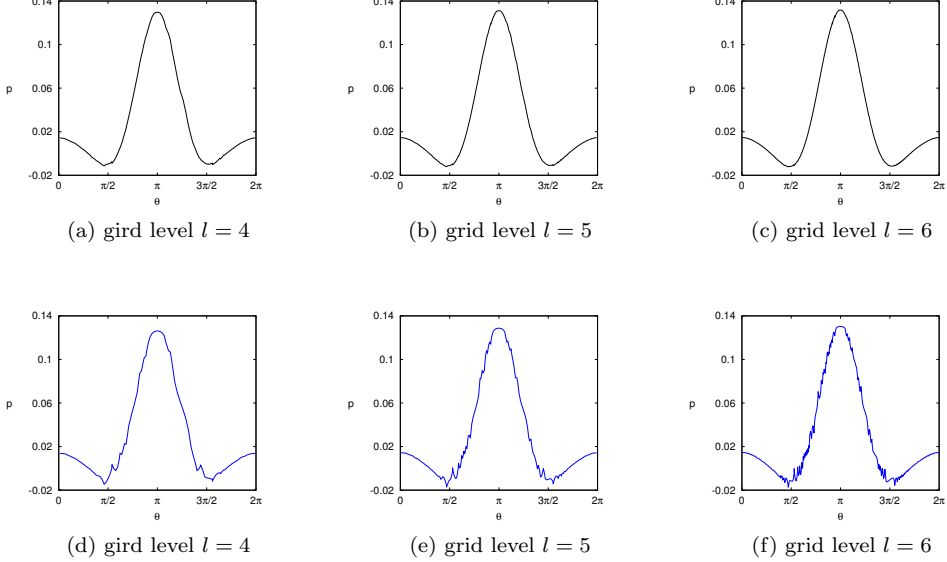


Figure 12: Pressure along the interface $\gamma(\theta) := 0.05 (\cos(\theta), \sin(\theta))^T$ for different grid refinements. (a)-(c) no oscillations for the unfitted scheme with enrichment; (d)-(f) oscillations for the unfitted scheme without enrichment

asymptotic solution indicated by the black line in Fig. 13a and nicely converges towards it. Since the analytical solution is only asymptotically valid, i.e. for a sufficiently small radius, the distance between numerical and analytical solution increases for radii > 0.3 . The according plots for the quantities $\mathbf{U}_x(r)$ and $\omega(r)$ are depicted in Fig. 13b and 13c.

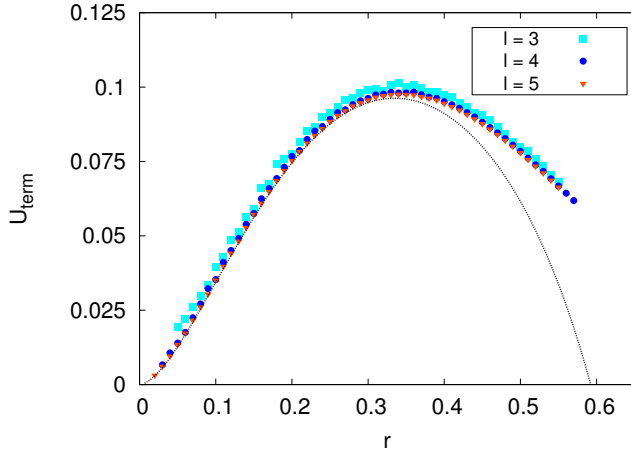
535 For comparison with the scheme without enrichment the corresponding results are shown in Fig. 14 based on the computations presented in [23]. The decreased accuracy can be observed and moreover, the unsteady course of the graph for the coarsest level 3 of Fig. 14 reveals a high dependence of the approximation quality on the radius, i.e. the position of the interface with respect to the grid.

540 Table 4 shows the discrete l^2 -norm

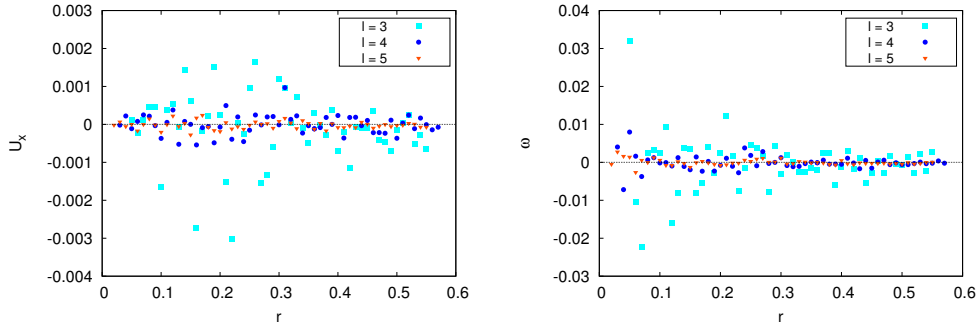
$$\epsilon_{\mathbf{U}_y} := \sqrt{\frac{1}{N_r} \sum_{i=1}^{N_r} [U_{\text{term}}(r_i) - \mathbf{U}_y(r_i)]^2}, \quad (32)$$

$$\epsilon_{\mathbf{U}_x} := \sqrt{\frac{1}{N_r} \sum_{i=1}^{N_r} \mathbf{U}_x(r_i)^2}, \quad \epsilon_\omega := \sqrt{\frac{1}{N_r} \sum_{i=1}^{N_r} \omega(r_i)^2}, \quad (33)$$

of the errors for all quantities $\mathbf{U}_y(r)$, $\mathbf{U}_x(r)$ and $\omega(r)$. It is $r_{i+1} - r_i = 0.01$ and N_r denotes the number of radii $r_i \in [0.02; 0.3]$, $i = 1, \dots, N_r$ for which the test problem was computed. As derived in [23] at least two vertices are required within P . Therefore, the admissible minimal radius and along with it the number N_r differ on each grid level.



(a) Falling velocity $\mathbf{U}_y(r)$ and asymptotic solution (black line), see (31).



(b) Velocity $\mathbf{U}_x(r)$; analytical solution (black line). (c) Rotation $\omega(r)$ and analytical solution (black line).

Figure 13: Particle velocities for varying radius r and different levels l of grid refinement.

Table 4 shows that the error decreases under refinement. Again, we also added the results for the case without enrichment presented in [23] showing a minor accuracy. It should be emphasized that the error is averaged over several radii. Since the quality of the approximation of the interface changes for each radius with respect to a given fixed refinement level of the grid, these measurements are not suitable to investigate the convergence properties of the scheme.

7.3. Validation of the angular component - rotating particle in linear shear flow

For the validation of the angular component of the particle velocity we conducted the simulation of linear shear flow between two walls in 2 and 3 dimensions. The particle is placed in the middle between two walls with distance D which move in opposite directions

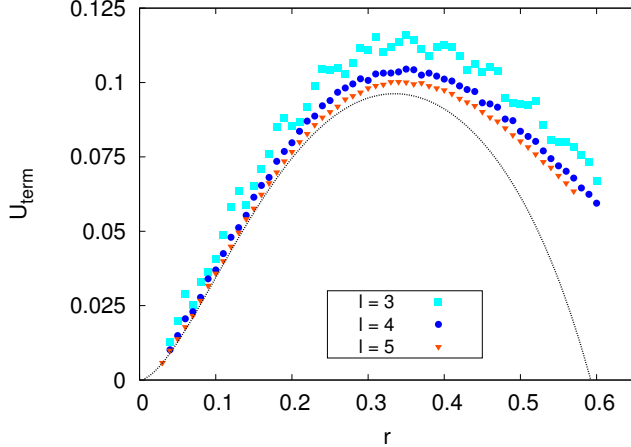


Figure 14: Falling velocity $\mathbf{U}_y(r)$ without enrichment, cf. [23], for varying radius r and different levels l of grid refinement and asymptotic solution (black line), see (31).

		with enrichment			without enrichment		
l	# DoFs	$\epsilon_{\mathbf{U}_y}$	$\epsilon_{\mathbf{U}_x}$	ϵ_ω	$\epsilon_{\mathbf{U}_y}$	$\epsilon_{\mathbf{U}_x}$	ϵ_ω
3	11,607	1.092e-02	9.159e-04	7.301e-03	2.762e-02	1.125e-03	1.447e-02
4	47,211	1.199e-02	2.642e-04	1.991e-03	2.063e-02	4.726e-04	4.843e-03
5	190,419	8.973e-03	1.045e-04	7.748e-04	1.303e-02	1.582e-04	1.866e-03

Table 4: L^2 -error for \mathbf{U}_y , \mathbf{U}_x and ω , see (32), (33).

555 to each other. For a shearing velocity u_S of one wall (and $-u_S$ of the opposite wall, respectively) the uniform shear rate in the steady state is given to $S := \frac{2}{d}u_S$ which yields a terminal angular velocity $\omega = 0.5S$ of the particle. Thus, it is appropriate to conduct the computations in a dimensionless setting. We apply Dirichlet boundary conditions on the outer boundary with u_S and $-u_S$ on the shearing walls and the corresponding linear profile along the remaining walls. The dimensions of the channel are 6×4 and $6 \times 4 \times 4$ which gives $D = 4$. For $u_S := 0.02$ the analytical solution for the particle is $\omega = 0.005$. Furthermore, we choose the parameter $\rho_f = \rho_P = 1.0$ and $\mu_f = 0.01$ in accordance with Wan and Turek [48] and Krause and Kummer [26] who conducted the same tests for the 2-dimensional case. As in [48] and [26] we will run the simulation for different particle sizes.

560

7.3.1. 2D-case

The simulations were conducted on the unstructured grid as depicted in Fig. 15 (left) with 419 715 degrees of freedom and the different radii $r = 0.3$, $r = 0.6$ and $r = 0.9$. The left column of Fig. 17 shows snapshots of the solution for $r = 0.3$. The time evolution 570 of the angular velocity for all three radii is plotted in Fig. 16 (left). The time until it reaches its equilibrium lies around $t \approx 200$. This is in good agreement with [48]. In



Figure 15: Computational domain for linear shear flow simulations in 2 and 3 dimensions.

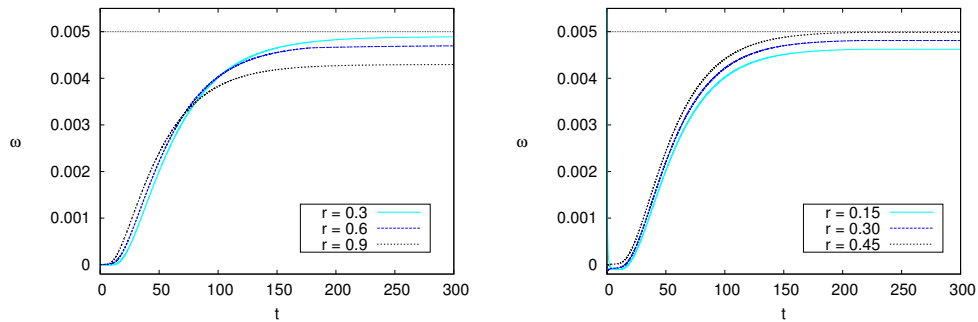


Figure 16: Time evolution of the angular velocity of a particle in linear shear flow with different radii for 2d computations (left) and 3d computations (right).

addition, a reference simulation without particle yielded a comparable time range.

The different radii cause different dynamics of the particle: For bigger particles the angular velocity deviates to a greater extent from the shear rate of the surrounding fluid. Presumably the smaller distance between particle and wall leads to a greater disturbance of the flow field. The same relation between radius and terminal velocity was observed in [48] and [26]. In contrast to their computations however, we observe a faster increase in rotation for bigger particles during the initial phase. Since no experiments can serve for comparison, we at least want to argue that again the smaller distance of bigger particles to the walls enables a faster transfer at the onset of the motion. Since the densities of the two phases were chosen identically, inertial effects can be largely excluded.

7.3.2. 3D-case

The 3-dimensional computations were performed on the unstructured grid as depicted in Fig. 15 (right) with 157 956 degrees of freedom and the different radii $r = 0.15$, $r = 0.3$ and $r = 0.45$. The right column of Fig. 17 shows snapshots of the solution for $r = 0.3$. The time evolution of the angular velocity for all three radii is plotted in Fig. 16 (right). In accordance to the 2-dimensional case the time until it reaches its equilibrium lies around $t \approx 200$.

Again, the different radii cause different dynamics of the particle. However, they differ from the dynamics observed for the 2-dimensional tests: First of all, as to be expected

for bigger particles, their acceleration at the onset of the wall movement is faster than for smaller particles. The same behaviour was already observed in 2 dimensions. However, the relation between radius and terminal velocity is inverted. A possible explanation is the surface-to-volume-ratio which is $A_d/V_d = d r^{-1}$, with radius r and $d = 2, 3$ for the spatial dimension, respectively. Therefore, in 3 dimensions the relative surface is bigger. Since the transfer of forces is mediated by the surface, we argue that the disturbance due to the wall has smaller effect in the 3-dimensional case.

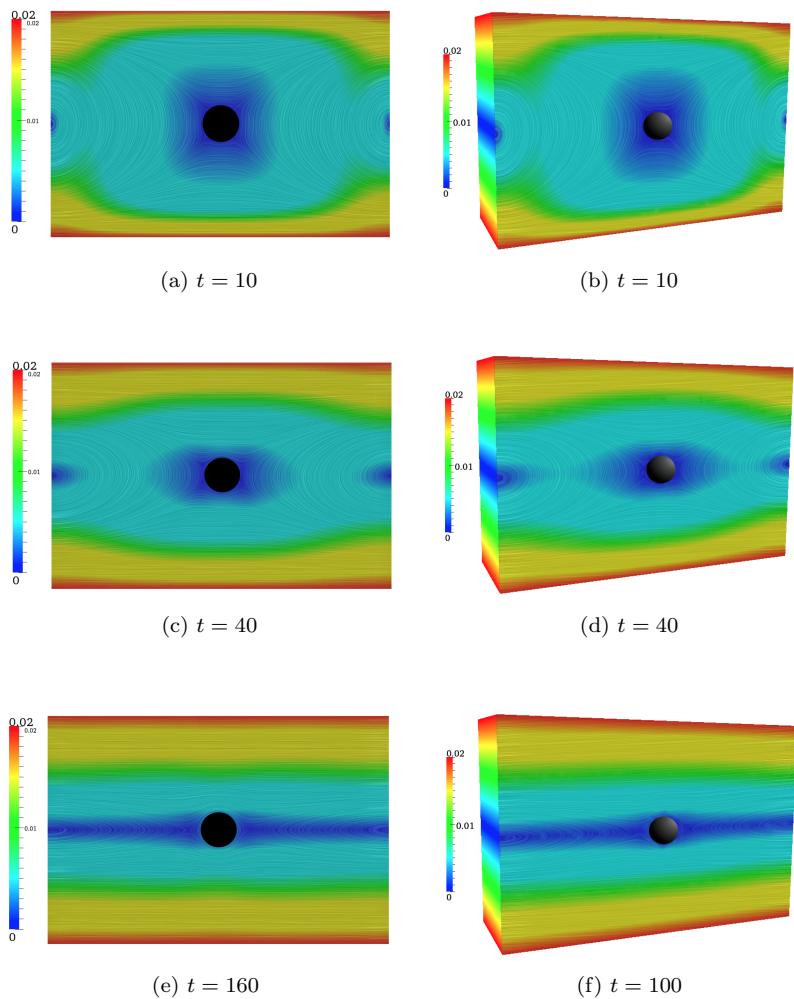


Figure 17: Magnitude of the velocity (color) and streamlines for a rotating particle in 2 dimensional (left column) and 3 dimensional (right column) linear shear flow.

7.4. Instationary benchmark of a sedimenting particle

A very famous benchmark test for particulate flow is the sedimentation of a particle.
600 It has been studied in the literature for 2 dimensions by Wan and Turek [48], Blasco et al.
[5], Krause and Kummer [26] and for 3 dimensions by ten Cate et al. [39]. Beside the
terminal velocity, being already studied in Section 7.2, the acceleration and deceleration
account for a suitable coupling in time. Our fully-implicit scheme was applied to both
scenario.

605 **7.4.1. 2D-case**

One sedimenting circular particle: The benchmark was already studied for our
scheme without enrichment, cf. [23]. We will compare the different results. The computa-
tional domain is a channel with dimensions $H \times L = 2 \times 6$ as for the stationary case
in Section 7.2. As parameter for the particle and the fluid we set $r = 0.125$, $\rho_P = 1.25$,
610 $\rho_f = 1.0$ and $\mu = 0.1$. No-slip Dirichlet conditions are applied on the outer boundary
and initially the particle is at rest and at position $(1, 2)$. For comparison of our results
we refer to [13]. The same computations were also carried out by Wan and Turek [48],
Blasco et al. [5] and Krause and Kummer [26].

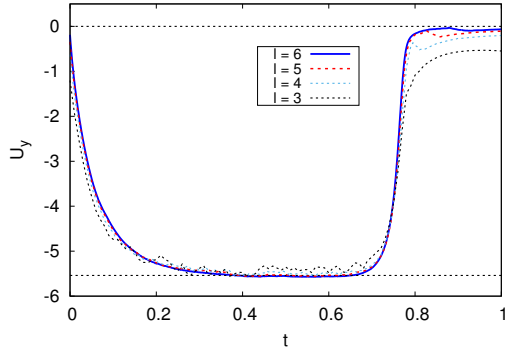
The benchmark was computed for 4 refinement levels $l = 3, \dots, 6$. The time step was
615 refined accordingly ranging from $\Delta t = 1 \cdot 10^{-2}$ to $1.25 \cdot 10^{-3}$.

Fig. 19 shows snapshots of the computed velocity field on grid level 5 for different
points in time. Fig. 18 shows the temporal evolution of the y -component of the trans-
lational velocity and the y -coordinate of the center of mass. The dashed lines indicate
620 the reference value $U_{\text{term}} = 5.5392$ according to [13]. The bad resolution of the inter-
face on the coarsest level leads to oscillations in the falling velocity $\mathbf{U}_y(t)$. The same
behaviour was already observed in [23] for the scheme without enrichment. However,
already on level 4 the velocity evolves smoothly, in contrast to the previous results. Un-
der refinement the terminal velocity converges to the reference value. The exact data is
625 summarized in Table 5 together with the Reynolds number derived from the terminal
velocity. For the computation of U_{term} the values of $\mathbf{U}_y(t)$ were averaged within the time
interval $[0.4, 0.6]$. The Reynolds number is also in good agreement with those computed
in [13], $\text{Re} = 17.31$, in [48], $\text{Re} = 17.15$ and in [5], $\text{Re} = 17.34$.

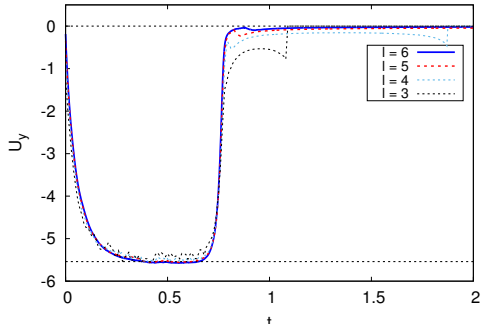
l	# DoFs	U_{term}	Re
3	11,607	5.4164	16.93
4	47,211	5.4941	17.17
5	190,419	5.5441	17.33
6	771,171	5.5611	17.38
Reference		5.5392	17.31

Table 5: Terminal velocity and Reynolds number of a sedimenting particle and reference,
cf. [13]

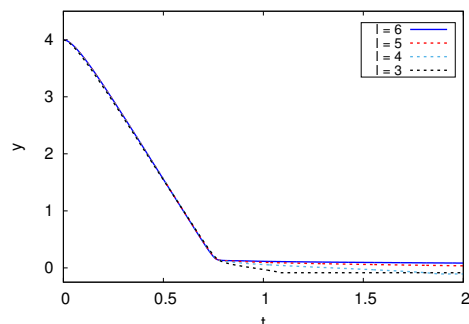
It should be emphasized that not only the terminal velocity itself but also the whole
time evolution of the falling velocity is in good agreement with those computed in [48]
630 and [5]. The important features of a fast accelerating and decelerating phase are captured
well by our fully-coupled scheme. In particular, the deceleration runs without overshoot



(a) Evolution of the falling velocity $\mathbf{U}_y(t)$



(b) Prolonged evolution of the falling velocity $\mathbf{U}_y(t)$



(c) Evolution of the y-coordinate of particle center

Figure 18: Time evolution of a sedimenting particle; (b) illustrates the stable phase of the particle at rest.

across the ground. That can be attributed to an efficient coupling between the particle degrees of freedom and those at the outer boundary. Of course a suitable size of the time step is necessary. However, we want to recall that no additional repellent forces were applied. Many discrete scheme implement a collision force commonly depending on the distance to the wall to avoid a collision of the immersed boundary with the ground, cf. [15], [48], [44], [46], [1], [5], [51] and [26]. Finally, the simulation reaches a stable equilibrium in which the particle stays at rest.

A further quality of our scheme is a certain conservative property: Since solving the coupled system of particle and fluid is conducted in one single step without application of a time splitting scheme the interaction forces are instantaneously exchanged between fluid and particle without loss of momentum. After acceleration has stopped and before the particle gets decelerated by the ground the particle is in full equilibrium and falls with constant velocity. Our scheme can reproduce that since for $t \in [0.3, 0.7]$ the graph follows a horizontal line as would be expected. Therefore, the particle is also in a *numerical*

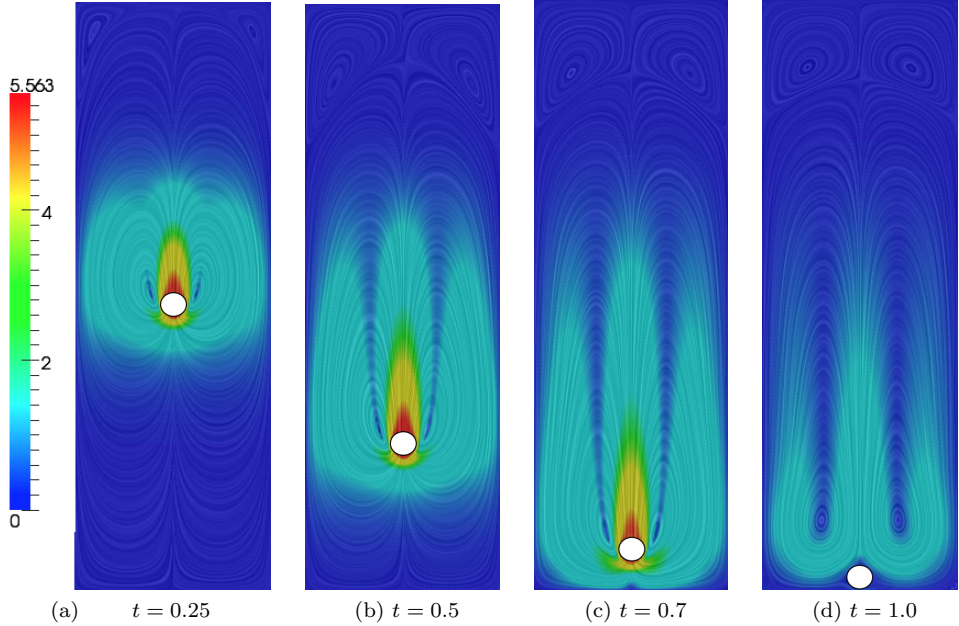


Figure 19: Sedimenting particle at $\text{Re} \approx 17$: Magnitude of the velocity (color) and streamlines for different times computed on level $l = 5$.

equilibrium.

Finally, we studied the convergence of our scheme. For this purpose, we evaluated the L^2 -error

$$\epsilon_{\mathbf{U}_x} := \sqrt{\frac{1}{N_t} \sum_{i=1}^{N_t} \mathbf{U}_x(t_i)^2}, \quad \epsilon_\omega := \sqrt{\frac{1}{N_t} \sum_{i=1}^{N_t} \omega(t_i)^2} \quad (34)$$

for the horizontal and rotational velocity whose analytical solution is zero. We considered the period of $T = 1.5s$ and therefore $N_t := T/\Delta t$ denotes the number of time steps taken into account for the averaging. It is $t_{i+1} = t_i + \Delta t$. The results are summarized in Fig. 20. Due to a sufficiently small time step we can observe a rate near to second order.

650

Three sedimenting circular particles: As mentioned in the introduction of Section 2.1, it is straight forward to include further particles into the discretisation scheme. Beyond the benchmarks for validation, we shall present a more dynamical scenario. We simulated three identical particles with Reynolds number $\text{Re} \approx 270$.

655

The computational domain is the same as for the single falling particle. The fluid density and viscosity is $\rho_f = 1.0$ and $\mu = 0.01$. As parameter for all three particles we set $r = 0.09$ and $\rho_P = 1.5$. No-slip Dirichlet conditions are applied on the outer boundary and initially the particles are at rest and at the positions $(1.1, 1.0)$ for particle 660 1, $(0.6, 1.4)$ for particle 2 and $(1.5, 2.0)$ for particle 3, i.e. numbered by their positioning

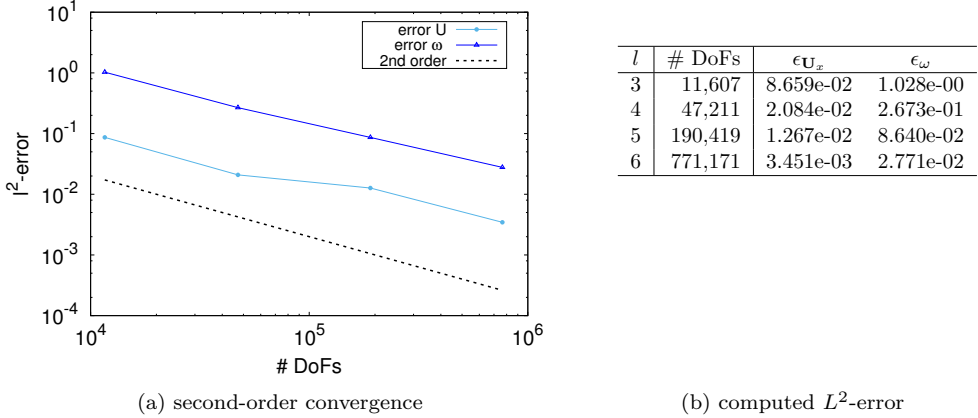


Figure 20: L^2 -error for $\mathbf{U}_x(t)$ and $\omega(t)$, see (34).

in y-direction. The test scenario was computed for 3 refinement levels $l = 4, 5, 6$. The time step was refined accordingly ranging from $\Delta t = 1 \cdot 10^{-3}$ to $2.5 \cdot 10^{-4}$.

Figures 21 (a)-(c) show respectively the temporal evolution of the y - and x -coordinate of the center of mass and the y -component of the translational velocity. The blue curves represent particle 1, which is falling behind the two others. We expect that its motion is influenced most by the turbulence induced by the motion of the other particles. Accordingly, its x -coordinate and velocity oscillates, as depicted in Fig. 21 (b), (c). Fig. 22 shows snapshots of the computed velocity field on grid level 6 for different points in time. The first two snapshots are taken just before and after the first peak of the blue curve in Fig. 21 (b). The last two snapshots are taken just before and after the third peak.

In order to demonstrate the grid convergence, the velocities of the three particles depicted in Fig 21 (c) are replotted in Figures 21 (d)-(f), but separately for each particle and for different refinements. We want to mention the slightly differing behaviour of the oscillating particle 1 (see Fig. 21 (d)) on the coarsest level 4 compared to level 5 and 6, indicating that the physics are not yet resolved correctly.

The maximal velocity $|\mathbf{U}_y| \approx 10$ yields a Reynolds number $\text{Re} := 2r\rho_P|\mathbf{U}_y|/\mu \approx 270$.

7.4.2. 3D-case

For the 3-dimensional benchmark numerical simulations and experimental data are provided by ten Cate et al. [39] and will serve for the validation. The computational domain is a channel with dimensions $0.1\text{m} \times 0.1\text{m} \times 0.16\text{m}$. A sphere with radius $r = 0.075\text{m}$ and density $\rho_p = 1.120 \frac{\text{kg}}{\text{m}^3}$ is placed at position $(0.05\text{m}, 0.05\text{m}, 0.12\text{m})$ for its center and is initially at rest. The parameter for the fluid are $\rho_f = 970 \frac{\text{kg}}{\text{m}^3}$ and $\mu = 373 \frac{\text{Ns}}{\text{m}^2}$ for the dynamic viscosity, in accordance with [39].

The computations were performed on a structured, simplicial mesh on 3 refinement levels $l = 2, 3, 4$ and with accordingly refined time step size $\Delta t = 4 \cdot 10^{-3}\text{s}$, $\Delta t = 2 \cdot 10^{-3}\text{s}$

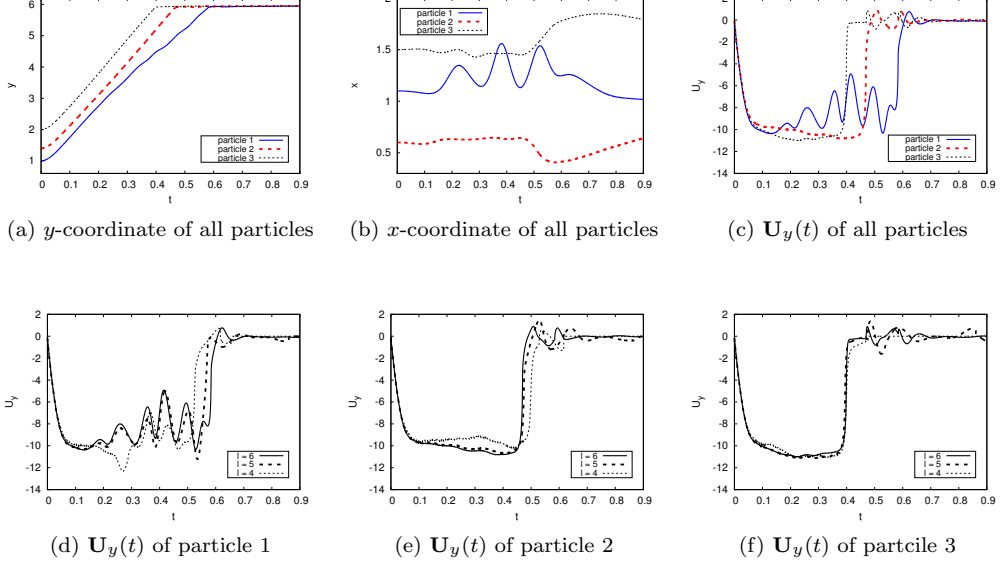


Figure 21: Time evolution of three sedimenting particles; (a)-(c) y - and x -coordinate of the center of mass and the y -component of the translational velocity $\mathbf{U}_y(t)$ for all three particles; (d)-(f) y -component of the translational velocity $\mathbf{U}_y(t)$ of each particle separately and for all three levels of refinement.

and $\Delta t = 1 \cdot 10^{-3} s$. Fig. 24 shows snapshots of the magnitude of the velocity computed on level 4. The evolution of the falling velocity \mathbf{U}_y and the y -coordinate of the particle center over time are plotted in Fig. 23. The reference by [39] for the terminal velocity ($U_{\text{term}} = 0.038 \frac{m}{s}$) is marked by the horizontal, dashed line. As already described in detail for the 2-dimensional test case, the different phases of acceleration, equilibrium and deceleration are captured well. Also the final state of a resting particle is depicted in the prolonged plot of Fig. 23b. Since the resolution of level 2 does not provide a good approximation, the velocity is very unsteady in time. However, the oscillations get smoothed out under refinement. The L^2 -error for the remaining velocity components of the particle is summarized in Table 6.

l	# DoFs	$\epsilon_{\mathbf{U}_x}$	$\epsilon_{\mathbf{U}_z}$	ϵ_{ω_x}	ϵ_{ω_y}	ϵ_{ω_z}
2	28,900	1.295e-03	1.159e-03	1.313e-02	1.955e-02	1.921e-02
3	213,444	1.036e-03	9.332e-04	1.581e-02	1.848e-02	1.442e-02
4	1,639,300	4.352e-04	3.269e-04	5.841e-03	5.358e-03	6.368e-03

Table 6: L^2 -error for \mathbf{U}_x , \mathbf{U}_z , $\boldsymbol{\omega}_x$, $\boldsymbol{\omega}_y$ and $\boldsymbol{\omega}_z$, see (34).

8. Conclusions

The motivation for the development of the described immersed boundary method was
 700 the elimination of pressure oscillations as observed in earlier particulate flow simulations,
 cf. [23]. Since previous implementations employing ghost fluid techniques could not
 eliminate the oscillations, the developed method was aimed to approximate the gradient
 and along with it the direction of the normal forces acting on the interface with higher
 accuracy. The formulation as Petrov-Galerkin FVM enabled the derivation of suitably
 705 enriched spaces. Furthermore, by means of the identification (16) we could derive the
 according Galerkin FEM which simply turned out to be a FEM on the adaptively refined
 mesh \mathcal{T}_h^* .

The interpretation of the FEM as Petrov-Galerkin FVM and the [adaptation](#) of the
 test space therefore yields an appropriate weak formulation of the boundary conditions.
 710 This proceeding was already exploited for the formulation of the RBM constraint derived
 in [23]. We emphasize that for both tasks - which is in [23] the imposition of the special
 boundary condition of RBM on ∂P and in this work the formulation of a boundary
 condition on an immersed interface - a *new* conditional equation was derived. In contrast,
 common approaches usually utilise the given equation for the boundary condition and
 715 derive the weak formulations from it: For example, the weak formulation of Nitsche [32]
 directly test the given boundary equations by means of $([\alpha \nabla u \cdot \mathbf{n}], v)_\Gamma = 0$ and the weak
 form in Glowinski et al. [15] introduces the equation $(\mathbf{u} - [\mathbf{U} + \boldsymbol{\omega} \times \mathbf{r}(\vec{x})], \boldsymbol{\mu}) = 0$. The
 key of our approach is the suitable adaptation and extension of the test space which

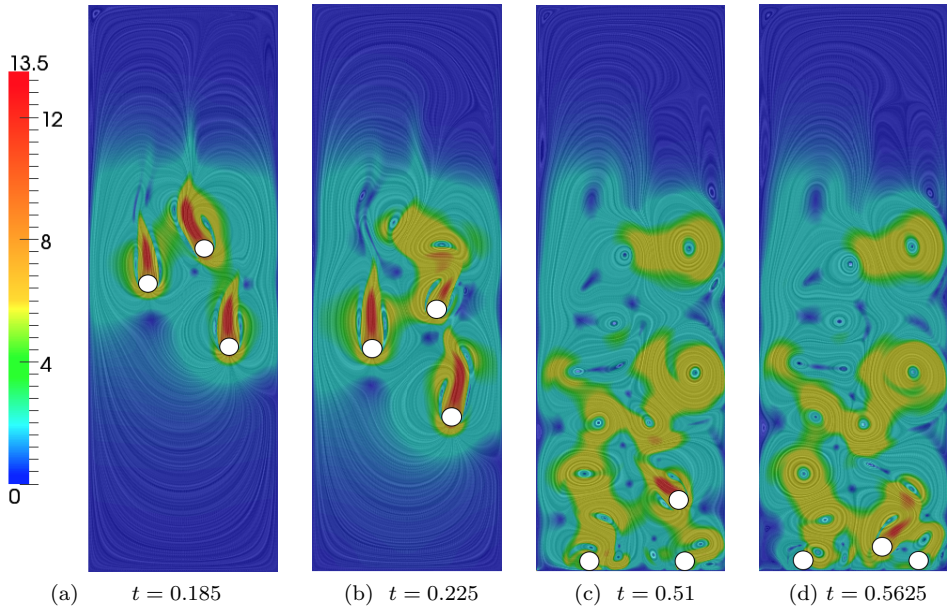
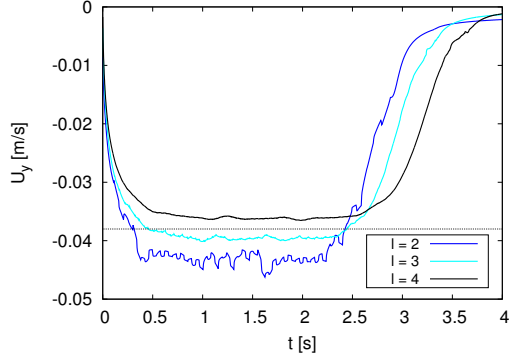
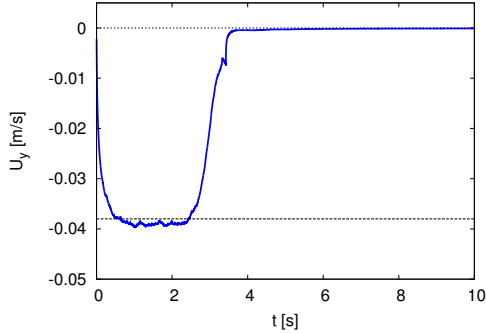


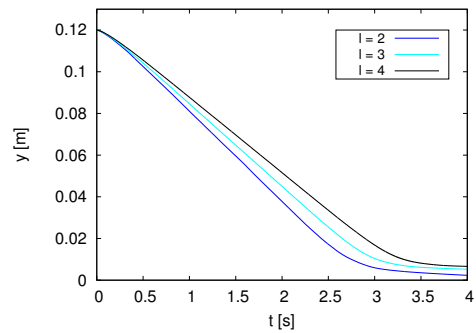
Figure 22: Three sedimenting particles at $\text{Re} \approx 270$: Magnitude of the velocity (color)
 and streamlines for different times computed on level $l = 6$.



(a) Evolution of the falling velocity $\mathbf{U}_y(t)$



(b) Prolonged evolution of the falling velocity $\mathbf{U}_y(t)$



(c) Evolution of the y-coordinate of particle center

Figure 23: Time evolution of a sedimenting sphere; (b) illustrates the stable phase of the particle at rest.

naturally generates new and physically meaningful conditioning equations.

In summary, a finite volume formulation can on the one hand facilitate the formulation of given boundary forces. On the other hand, finite element theory provides tools for the construction of mathematically favourable schemes. As already pursued by the introduction of rotational spaces in [23] the strategy of combining both approaches can be useful in order to construct good numerical schemes.

Since the forces along an immersed boundary become even more relevant in the case of deformable interfaces, the next step will be the application of the derived approach to problems with more than one liquid phase.

Acknowledgements

The authors are grateful to D. Logaschenko for the useful discussions and thank A. Vogel and S. Reiter for their support with the implementation in *UG4*.

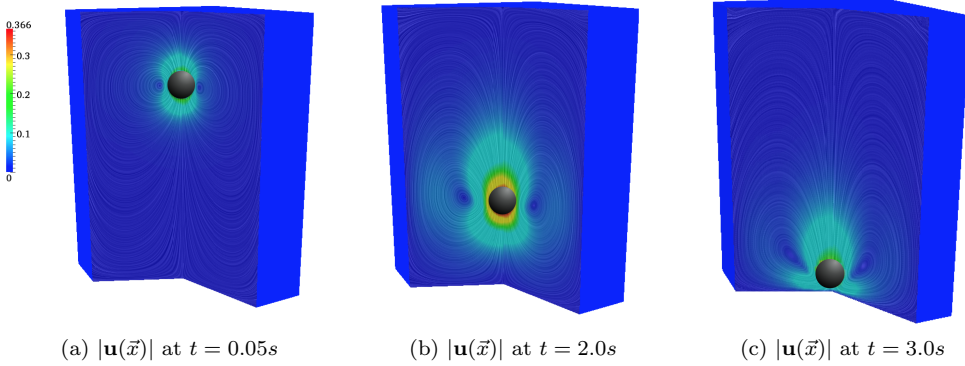


Figure 24: Sedimenting sphere: Magnitude of the velocity (color) and streamlines for different times.

References

- [1] S. V. Apte, M. Martin, and N. A. Patankar. A numerical method for fully resolved simulation (FRS) of rigid particle-flow interactions in complex flows. *Journal of Computational Physics*, 228(8):2712–2738, 2009.
- [2] R. Ausas, G. Buscaglia, and S. Idelsohn. A new enrichment space for the treatment of discontinuous pressures in multi-fluid flows. *International Journal for Numerical Methods in Fluids*, 70:829–850, 2012.
- [3] R. E. Bank and D. J. Rose. Some Error Estimates for the Box Method. *SIAM Journal on Numerical Analysis*, 24:777–787, 1987.
- [4] R. Becker, E. Burman, and P. Hansbo. A Nitsche extended finite element method for incompressible elasticity with discontinuous modulus of elasticity. *Computer Methods in Applied Mechanics and Engineering*, 198:3352–3360, 2009.
- [5] J. Blasco, M. C. Calzada, and M. Marín. A Fictitious Domain, parallel numerical method for rigid particulate flows. *Journal of Computational Physics*, 228(20):7596–7613, 2009.
- [6] W.-P. Breugem. A second-order accurate immersed boundary method for fully resolved simulations of particle-laden flows. *Journal of Computational Physics*, 231(13):4469–4498, 2012.
- [7] E. Burman and M. A. Fernandez. Stabilization of explicit coupling in fluid-structure interaction involving fluid incompressibility. *Computer Methods in Applied Mechanics and Engineering*, 198(5–8):766–784, 2009.
- [8] L. Chen. Finite Volume Methods. *private Communication*, 2010. <http://www.math.uci.edu/~chenlong/226/FVM.pdf>.
- [9] L. Chen, H. Wei, and M. Wen. An interface-fitted mesh generator and virtual element methods for elliptic interface problems. *Journal of Computational Physics*, 334:327–348, 2017.
- [10] J. Chessa and T. Belytschko. An Extended Finite Element Method for Two-Phase Fluids. *Journal of Applied Mechanics*, 70:12–17, 2003.
- [11] R. P. Fedkiw, T. Aslam, B. Merriman, and S. Osher. A Non-oscillatory Eulerian Approach to Interfaces in Multimaterial Flows (the Ghost Fluid Method). *Journal of Computational Physics*, 152:457–492, 1999.
- [12] I. Ginzburg and G. Wittum. Two-Phase Flows on Interface Refined Grids Modeled with VOF, Staggered Finite Volumes, and Spline Interpolants. *Journal of Computational Physics*, 166:302–335, 2001.
- [13] R. Glowinski. *Finite element methods for incompressible viscous flow*, pages 3–1176. Handbook of Numerical Analysis IX, North-Holland, Amsterdam. 2003.
- [14] R. Glowinski, T.-W. Pan, T. I. Hesla, and D. D. Joseph. A distributed Lagrange multiplier/fictitious domain method for particulate flows. *International Journal of Multiphase Flow*, 25:755–794, 1999.

- [15] R. Glowinski, T.-W. Pan, T. I. Hesla, D. D. Joseph, and J. Périaux. A Fictitious Domain Approach to the Direct Numerical Simulation of Incompressible Viscous Flow past Moving Rigid Bodies: Application to Particulate Flow. *Journal of Computational Physics*, 169(2):363–426, 2001.
- [16] S. Gross and A. Reusken. An extended pressure finite element space for two-phase incompressible flows with surface tension. *Journal of Computational Physics*, 224(1):40–58, 2007.
- [17] S. Gross, T. Ludescher, M. Olshanskii, and A. Reusken. Robust Preconditioning for XFEM Applied to Time-Dependent Stokes Problems. *SIAM Journal of Scientific Computing*, 38(6):A3492–A3514, 2016.
- [18] W. Hackbusch. On First and Second Order Box Schemes. *Computing*, 41(4):277–296, 1989.
- [19] A. Hansbo and P. Hansbo. An unfitted finite element method, based on Nitsche's method, for elliptic interface problems. *Computer Methods in Applied Mechanics and Engineering*, 191(47-48):5537–5552, 2002.
- [20] P. Hansbo, J. Hermansson, and T. Svedberg. Nitsche's method combined with space-time finite elements for ALE fluid-structure interaction problems. *Computer Methods in Applied Mechanics and Engineering*, 193(39-41 SPEC. ISS.):4195–4206, 2004.
- [21] P. Hansbo, M. G. Larson, and S. Zahedi. A cut finite element method for a Stokes interface problem. *Applied Numerical Mathematics*, 85:90–114, 2014.
- [22] S. Höllbacher. *Voll gekoppelte Modellierung zur direkten numerischen Simulation partikulärer Fluide*. PhD thesis, Universität Frankfurt, 2016.
- [23] S. Höllbacher and G. Wittum. Rotational test spaces for a fully-implicit FVM and FEM for the DNS of particulate flows. *TBA*, 2018.
- [24] V. John and G. Matthies. Higher-order finite element discretizations in a benchmark problem for incompressible flows. *International Journal for Numerical Methods in Fluids*, 37:885–903, 2001.
- [25] M. Kirchhart, S. Gross, and A. Reusken. Analysis of an XFEM Discretization for Stokes Interface Problems. *SIAM Journal of Scientific Computing*, 38(2):A1019–A1043, 2017.
- [26] D. Krause and F. Kummer. An incompressible immersed boundary solver for moving body flows using a cut cell discontinuous Galerkin method. *Computers and Fluids*, 153:118–129, 2017.
- [27] C. Lehrenfeld. *On a Space-Time Extended Finite Element Method for the Solution of a Class of Two-Phase Mass Transport Problems*. PhD thesis, Universität Aachen, 2015.
- [28] C. R. Liu. On Partitions of Unity Property of Nodal Shape Functions: Rigid-Body-Movement Reproduction and Mass Conservation. *International Journal of Computational Methods*, 13:1–13, 2016.
- [29] R. Mittal and G. Iaccarino. Immersed Boundary Methods. *Annual Review of Fluid Mechanics*, 37(1):239–261, 2005.
- [30] N. Moës, J. Dolbow, and T. Belytschko. A finite element method for crack growth without remeshing. *International Journal for Numerical Methods in Engineering*, 46:131–150, 1999.
- [31] S. Nägele. *Mehrgitterverfahren für die inkompressiblen Navier-Stokes Gleichungen im laminaren und turbulenten Regime unter Berücksichtigung verschiedener Stabilisierungsmethoden*. PhD thesis, Universität Heidelberg, 2003.
- [32] J. Nitsche. Über ein Variationsprinzip zur Lösung von Dirichlet-Problemen bei Verwendung von Teilräumen, die keinen Randbedingungen unterworfen sind. *Abh. a.d. Math. Sem. Univ. Hamburg*, 36:9–15, 1971.
- [33] M. Oevermann, C. Scharfenberg, and R. Klein. A sharp interface finite volume method for elliptic equations on Cartesian grids. *Journal of Computational Physics*, 228:5184–5206, 2009.
- [34] C. S. Peskin. Numerical Analysis of Blood Flow in the Heart. *Journal of Computational Physics*, 25:220–252, 1977.
- [35] A. Reusken. Analysis of an extended pressure finite element space for two-phase incompressible flows. *Computing and Visualization in Science*, 11(4-6):293–305, 2008.
- [36] H. Sauerland and T. Fries. The stable XFEM for two-phase flows. *Computers and Fluids*, 87:41–49, 2013.
- [37] M. Schäfer and S. Turek. Benchmark Computations of Laminar Flow Around a Cylinder. *Flow Simulation with High-Performance Computers II*, Band 2 von *Notes on Numerical Fluid Mechanics*: 547–566, 1996.
- [38] M. A. Schweizer. Stable Enrichment and Local Preconditioning in the Particle-Partition of Unity Method. *Numerische Mathematik*, 118:137–170, 2011.
- [39] A. ten Cate, C. H. Nieuwstad, J. J. Derksen, and H. E. A. Akker. Particle imaging velocimetry experiments and lattice-Boltzmann simulations on a single sphere settling under gravity. *Physics of Fluids*, 14:4012–4025, 2002.
- [40] T.-K. Tornberg and B. Engquist. Regularization techniques for numerical approximation of PDES

- 825 with singularities. *Journal of Scientific Computing*, 19:527–552, 2003.
- [41] T.-K. Tornberg and B. Engquist. Numerical approximations of singular source terms in differential equations. *Journal of Computational Physics*, 200:462–488, 2004.
- [42] S. Tschigale, T. Kempe, and J. Fröhlich. A non-iterative immersed boundary method for spherical particles of arbitrary density ratio. *Journal of Computational Physics*, 339:432–452, 2017.
- 830 [43] M. Uhlmann. An immersed boundary method with direct forcing for the simulation of particulate flows. *Journal of Computational Physics*, 209(2):448–476, 2005.
- [44] C. Veeramani, P. D. Minev, and K. Nandakumar. A fictitious domain formulation for flows with rigid particles: A non-Lagrange multiplier version. *Journal of Computational Physics*, 224(2):867–879, 2007.
- 835 [45] A. Vogel, S. Reiter, M. Rupp, A. Nägel, and G. Wittum. UG 4: A novel flexible software system for simulating PDE based models on high performance computers. *Computing and Visualization in Science*, 16:165–179, 2013.
- [46] A. Wachs. A DEM-DLM/FD method for direct numerical simulation of particulate flows: Sedimentation of polygonal isometric particles in a Newtonian fluid with collisions. *Computers and Fluids*, 38(8):1608–1628, 2009.
- 840 [47] G. J. Wagner, N. Moës, W. K. Liu, and T. Belytschko. The extended finite element method for rigid particles in Stokes flow. *International Journal for Numerical Methods in Engineering*, 51:293–313, 2001.
- [48] D. Wan and S. Turek. Direct numerical simulation of particulate flow via multigrid FEM techniques and the fictitious boundary method. *International Journal for Numerical Methods in Fluids*, 51(5):531–566, 2006.
- [49] F. Wang, Y. Xiao, and J. Xu. High-Order Extended Finite Element Methods for Solving Interface Problems. *Numerical Analysis*, pages 1–25, 2016.
- 845 [50] J. Xu and Q. Zou. Analysis of linear and quadratic simplicial finite volume methods for elliptic equations. *Numerische Mathematik*, 111(3):469–492, 2009.
- [51] J. Yang and F. Stern. A non-iterative direct forcing immersed boundary method for strongly-coupled fluid-solid interactions. *Journal of Computational Physics*, 295:779–804, 2015.
- [52] X. Ye. On the Relationship Between Finite Volume and Finite Element Methods Applied to the Stokes Equations. *Numerical Methods for Partial Differential Equations*, 17:440–453, 2001.